UNCOVERING ATOMIC STRUCTURES IN TWO-DIMENSIONAL LATERAL HETEROJUNCTIONS

A Dissertation

Presented to the Faculty of the Graduate School

of Cornell University

in Partial Fulfillment of the Requirements for the Degree of

Doctor of Philosophy

by

Yimo Han

May 2018

UNCOVERING ATOMIC STRUCTURES IN TWO-DIMENSIONAL LATERAL HETEROJUNCTIONS

Yimo Han, Ph.D.

Cornell University 2018

Two-dimensional layered crystals are a promising class of materials for post silicon electronics. Due to their atomic thinness, flexibility, and versatile electrical properties (i.e. conductors, semiconductors, and insulators), we can envision future ultra-small, flexible computers completely comprised of various two-dimensional materials. For this application, lateral heterostructures of two-dimensional materials play a major role in the realization of wholly two-dimensional devices, as they are the fundamental elements in a circuit, such as *p*-*n* junctions and metal-semiconductor contacts.

This dissertation will employ transmission electron microscopy and related techniques to address how different two-dimensional materials merge to form lateral heterostructures, specifically between two distinct two-dimensional semiconductors (analogous to *p*-*n* junctions) and two-dimensional conductor-semiconductor heterostructures (analogous to metal-semiconductor contacts). Within the heterostructures between two semiconductors, Chapter 2 and 3 will discuss atomically sharp interfaces and gradual interfaces in lateral heterostructures, respectively. Chapter 4 will describe the conductor-semiconductor interconnects between two-dimensional materials with dissimilar lattice structures. Our results demonstrate how the strain is relaxed in epitaxial lateral heterostructures, as well as how the heterostructure between crystallographically distinct two-dimensional materials forms. These findings can unravel how to

use or engineer distortions in two-dimensional lateral heterojunctions, predict the mechanical strength and devices performance, and inform the mechanism of chemical synthesis at the interface between atomically thin films.

BIOGRAPHICAL SKETCH

Yimo Han was born in Beijing, China to a family of artists in 1989. Her father is a professor and dean of the Department of Fine Arts at Capital Normal University in Beijing, while her mother is a retired art teacher who now focuses on creating artwork. In Yimo's youth, her parents wanted her to follow in their footsteps and become an architect or designer. However, Yimo developed a great interest in science and technology, a deviation from her parents' career that was fully respected and supported.

Not to disappoint them, Yimo showed great promise in physical sciences, joining the physics department in Tsinghua University, a top undergraduate program in China. During her undergraduate, she worked on carbon nanotubes, which would introduce her to the many other nanomaterials she would later work on. As a nod to her parents and her own background, she also became president of Tsinghua's Student Art Association, where she organized exhibitions and workshops. In 2012, Yimo received her Bachelor of Science degree in *Math and Physics*.

After living in Beijing for twenty-two years, she moved to Cornell University to pursue her Ph.D. in Applied Physics. Located in Ithaca, a town in upstate New York, winters at Cornell can last nearly half the year. Acclimating to the environment and culture took some time, but once she dedicated herself to research, she found a desire to explore the broad and new world of nanomaterials.

This document is dedicated to all Cornell graduate students.

ACKNOWLEDGEMENTS

During my Ph.D. I met so many people who were friendly, generous, and supportive. Without them, I am sure it would not have been possible to accomplish this dissertation.

I would first like to thank my advisor, Professor David A. Muller, from whom I have learned how to do research from idea conception to project completion. David has supported me both scientifically and financially, and given me significant amount of freedom to explore research topics and collaborations. Working for David, I developed my sense of research by pursuing truly important scientific problems and questions, and I learned to present my research to a broad audience. I am very grateful to have had the chance to work with and learn from him.

The members of the Muller research group are extremely kind and helpful. I want to thank all of our group members, each of whom made the group warm, entertaining, and productive. In particular, Pinshane Huang (now an assistant professor in UIUC) was my mentor when I first joined the group. I appreciate the time she took to train me to use microscopes and to teach me how to become a strong woman in science. Her words have encouraged me to follow in her footsteps, pursuing a career in academia in order to discover fascinating science. Many thanks to Kayla Nguyen, who has worked with me very closely on the airSEM project and the EMPAD strain mapping project. Her talent and enthusiasm always influence me. I also want to thank Robert Hovden, Megan Holtz, Elliot Padgett, and Zhen Chen, Paul Cueva, Celesta Chang, Michael Cao, and Ela Correa, who are really generous and helpful, sharing Matlab codes, microscope tips, and providing helpful discussions.

I would like to gratefully acknowledge Professor Jiwoong Park and Profes-

sor Paul McEuen, who as my committee members have spent their invaluable time on my exams and dissertation. Jiwoong has also been my second advisor and he was the one who first introduced me to the 2-D world. Paul has the magic to always bring a lot of fun and enthusiasm to scientific research in our conversations and his presentations. I appreciate both Jiwoong's and Paul's dramatic influence on me and my career plan.

I would not have been able to achieve my Ph.D. without all my fantastic collaborators. At Cornell, I have worked with the Park group, Jena group, Xing group, Gruner group, and McEuen group. I also want to thank my collaborators outside Cornell who I have worked with very closely: Professor Lain-Jong Li from KAUST, Professor Markus Buehler from MIT, Professor Xiang Zhang from UC Berkeley, Professor Jing Kong from MIT, and Professor Chih-Kang Shih from UT Austin. Special thanks to Mervin Zhao, Ming-Yang Li, Gang-Seob Jung, Rusen Yan, Kibum Kang, Ang-Yu Lu, Yutsung Tsai, Zhao Qin, Yunfan Guo, Hanyu Zhu, etc. I have learned so much from my collaborators and thank them again for trusting me and working with me.

Cornell has one of the best microscopy staff in the world. I want to thank John Grazul, Mick Thomas, and Mariena Ramos, who are so kind and knowledgeable. They not only take care of the microscopes for users, but also teach us how to use the microscopes, from introducing us to the basics to answering all of our technical questions. Their generosity, patience, and hard work are surely one of the most important factors for the success of Cornell's electron microscopy. Special thanks to Dr. Earl Kirkland, who is the expert on NION and multi-slide simulations. His book is so useful that everyone in our group keeps a copy on their shelf.

I would also like to thank Professor Lena Kourkoutis and her group mem-

bers. They provided tremendous help when the Titan Themis was first installed. Many thanks also to Bin Xu from FEI, who spent weeks at Cornell aligning the microscopes while answering my naive questions.

Last but not least, I owe an immeasurable debt of gratitude to my parents, who have supported me my entire life. During my Ph.D., their mental and financial support from far-away China has made my life in the US much easier. And the final thank-you goes to my fiance, Mengnan Zhao: for loving me, for sharing so many unforgettable moments with me, and for supporting my career without any hesitation.

TABLE OF CONTENTS

LIST OF TABLES

LIST OF FIGURES

CHAPTER 1

INTRODUCTION

1.1 Two-dimensional materials

The integrated circuit that made computing ubiquitous has been one of the most important inventions in the modern era. Due to the scaling of Moore's law [1], where the transistor density on an integrated circuit roughly doubles every two years, humankind has seen massive leaps and bounds in information processing, analysis, and even artificial intelligence. As the transistor size is finite, technology has reached a point where new transistors must be less than 5 nanometers to continue the scaling of Moore's law. Conventionally, silicon has been the gold standard of electronic materials, giving birth to its eponymous valley, and has historically met the demands of transistor scaling. However, when bulk silicon is fabricated to nanometers in length, the switch-like behavior of the silicon transistor becomes increasingly poor, and ultimately will be difficult to utilize in electronic devices of the ultimate length scale which is required of Moore's law [1]. A potential, if idealized, solution to the problematic scaling of silicon has been in the usage of nanomaterials [2–5]. Nanomaterials, which are defined as any material with innate dimensions of nanometer scale, would have the lengths necessary to deal with Moore's law scaling as they themselves are the lengths of the required transistors. These nanomaterial transistors have seen potential success with enhanced performance or additional functionality when compared to traditional devices (as transistor channels, gate dielectrics, or conductive interconnects), though the costs, synthesis, and stability have all proven challenges for real-world industrial usage.

Among the most promising candidates for next-generation electronics are two-dimensional (2-D) materials. The atomically-thin 2-D films would theoretically allow for the ultimate scaling of transistors, while providing an advantage of transparency and compatibility with flexible substrates. Thus, these 2-D materials have become one of the most popular nanomaterials for electronics throughout the last decade. As there have been more and more 2-D materials discovered, containing conductors, insulators, and a wide range of semiconductors (with various band gaps and alignments), it is possible to envision some computer whose major material components are all 2-D materials.

The 2010 Nobel Prize in physics was awarded for graphene, the single layer of carbon atoms possessing extraordinary electrical properties [6–9]. Graphene can be achieved by just using adhesive Scotch tape to isolate the single layer (or a few layers) from bulk graphite [6–12]. Following graphene's example, many natural and chemically synthesized bulk crystals all used this form of micromechanical exfoliation using only tape to isolate a whole class of single-layered 2-D materials [13–17]. Even now, the usage of these micrometer-sized 2-D materials for devices is common and the discovery or demonstration of many extraordinary physical phenomena have used these "exfoliated" crystals, such as massless fermions [6], valley hall effect [15], super conductivity [17], and ideal transistor behaviors [14, 16].

However, the industrial viability of 2-D materials cannot possibly use micron sized flakes, but requires the "on-demand" synthesis of high quality wafer-scale crystals. Thus, the chemical synthesis, in particular the development of chemical vapor deposition (CVD, using both solid and gaseous precursors) have been extremely significant for the legitimization of 2-D materials, which can be grown

at the wafer scale [18–22]. In addition, the CVD process can create complicated structures that are impossible to produce using mechanical exfoliation, such as various heterostructures, which this dissertation will discuss in depth.

1.1.1 Graphene and transition metal dichalcogenides

Graphene, a monolayer of graphite (Fig. 1.1 a,b), is both the simplest (in theory and practice) and most widely studied 2-D material, due to the fact that it was the first isolated, has a rich amount of physics, is extremely chemically stable, and has excellent conductive properties. The existence and isolation of a single graphitic layer was controversial, as physicists in the 1930s such as Landau believed it to be thermodynamically unstable, due to the van der Waals force causing the single layer of atoms to fold upon itself [23]. However, in the 1960s, transmission electron microscopy studies showed that graphite down to nanometers in thickness (single- and few-layer graphene) could be mechanically isolated using the "Schotch Tape" method and stable [10–12]. It was not until 2000s that graphene caught the attention of the condensed matter community, as A. K. Geim and K. S. Novoselov were able to fabricate devices on exfoliated graphene (using the "Scotch Tape" method shown to them by their electron microscopy technician) and perform electric field measurements [7]. Demonstration of graphene's massless Dirac fermions and quantum Hall effect [6], consistent with ideal theoretical predictions, awarded the two the 2010 Nobel Prize in Physics. In 2008, a micrometer-sized crystal of monolayer graphene could sell for more than $1,000 [24]. Just two years later, chemical synthesis allowed for mass production, reducing the cost dramatically. This has allowed for industrial applications of these atomically thin films, such as 30-inch graphene

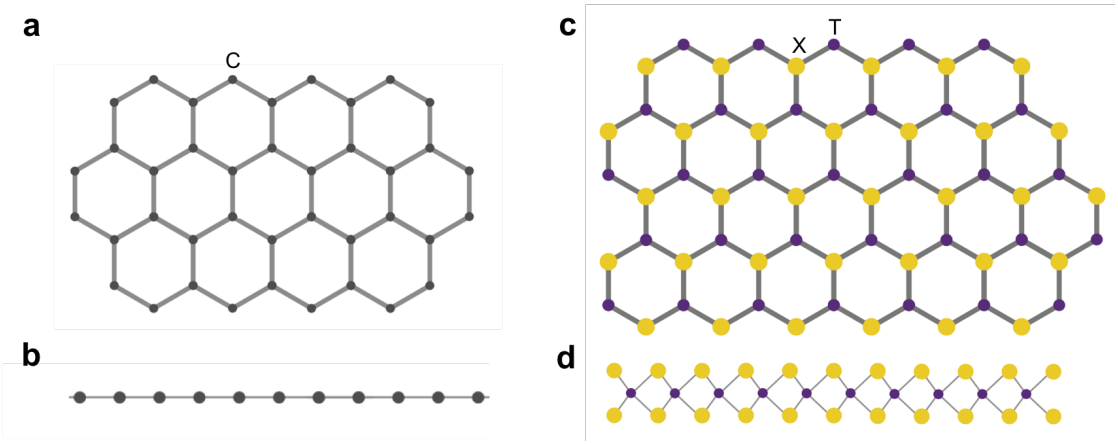

Figure 1.1: Lattice structures of 2-D materials. (a) Top-view projection of graphene which displays an obvious honeycomb lattice made of carbon atoms. (b) Side-view of graphene displaying the atomically-thin nature with one atom. (c) Top-view projection of the TMD (TX_2) showing a corresponding honeycomb lattice with alternating transition metal and chalcogen. (d) Side-view projection of the TMD showing the transition metal sandwiched by chalcogen atoms.

sheets for transparent electrodes [18].

Following in graphene's footsteps, in the early 2010s the family of transition metal dichalcogenides (TMDs) became of interest due to their semiconducting properties (whereas graphene is a semimetal, or a conductor) [14]. More interestingly, many TMDs transitioned from indirect to direct band gaps as the semiconductor was isolated from bulk to monolayer, even yielding photoluminescence [13]. These two properties both mean that the first 2-D electronics and optoelectronics could be realized by the same type of nanomaterials, quickly generating a massive amount of research efforts. Unlike graphene, the family of TMDs are a group of 2-D crystals with similar sandwiched structures of transition metals coordinated by chalcogens in a trigonal prismatic manner (Fig. 1.1 d), yielding three-atoms per molecular layer (no bonds between adjacent layers). From the top projection, the similarities with graphene become quite

Monolayer 2-D Materials	graphene	MoS_2	$MoSe_2$	WS_2	WSe_2
Lattice constants (Å)	2.46	3.18	3.32	3.18	3.32

Table 1.1: Lattice constants of 2-D materials. [25]

apparent, as both have a hexagonal honeycomb lattice (Fig. 1.1 a, c), with the TMD lattice constant mainly determined by chalcogen atom (table 1.1) [25].

Before proceeding, we must question why the atomic structures of 2-D materials are so important to understand or manipulate. The reason being that all throughout nature, in inorganic crystals or biological proteins, the structure is what determines the properties or functionality. The crystal structure or lattice distortion affects the electronic band structure, which ultimately affects the physical observables. More importantly, due to the reduced dimensionality, the influence of structure is even more apparent in 2-D materials, when compared with 3-D bulk materials. Studies of atomic distortions in 2-D materials, such as grain boundaries [26–28] and atomic defects [29–33] reveal local distortions to the atomic structure, corresponding to modifications to their optical and electrical properties. Thus, revealing the atomic structure is key to understanding the properties of 2-D materials and their composites.

1.1.2 Two-dimensional heterojunctions

Naturally, if we are to envision an "all 2-D" device, multiple 2-D materials must come into contact, forming various types of heterostructures or heterojunctions. Traditional heterojunctions (i.e. in bulk or 3-D), where two dissimilar crystalline materials seamlessly merge, have been widely used in high-speed-

and opto-electronics (2000 Nobel Prize in physics). Epitaxial growth methods, such as molecular beam epitaxy (MBE), have been developed to grow thin films of heterostructures, which can even approach 2-D. In these MBE grown heterojunctions with a finite lattice mismatch between the two crystals, a parameter called the *critical thickness* is used to describe the strain relaxation and dislocation formation at the heterointerfaces [34]. If the top film thickness is below the *critical thickness*, the thin film prefers to stay strained and form coherent heterostructure with the substrate (Fig. 1.2 a). Otherwise, a film thicker than the *critical thickness* cannot maintain the coherency due to the large strain energy, which is proportional to the film thickness. Instead, misfit dislocations start to form and travel to the heterointerfaces to relax the lattice strain (Fig. 1.2 b). This picture from the 3-D heterojunction model can be extended to describe 2-D heterojunctions.

There are two types of heterojunctions in 2-D materials: lateral heterojunctions where two dissimilar 2-D materials seamlessly merge in the lateral dimension, or vertical heterojunctions where the films tightly stack on top of each other. Both types of heterojunctions can be utilized in different ways and are important for future electronic applications. Thus far, atomically-thin *p*-*n* junctions [35–40], metal-semiconductor contacts [41–43], metal-insulator barriers [44–46], and semiconductor superlattices [47–50] have been demonstrated. When length scales reach a few nanometers, the atomic structures at the heterojunctions become essential as the effects of the lattice strain can drastically change the physical properties of the two materials. The lateral heterojunctions are more similar to what is traditionally observed in 3-D epitaxy, due to the formation of covalent bonds between the two materials, while the vertical ones are van der Waals (vdW) heterostructures [51] that contain a spontaneous strain re-

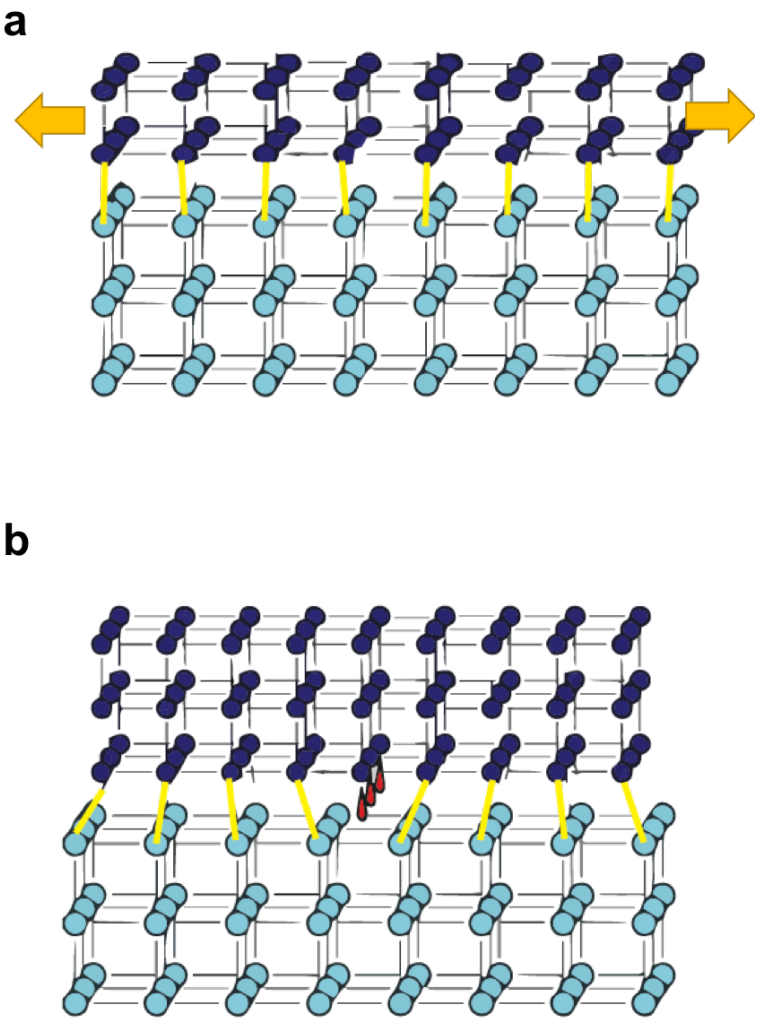

Figure 1.2: Schematic of heterostructures in bulk epitaxy. (a) Schematic of a coherent thin film, whose thickness is below the *critical thickness*. The thin film presents a uniaxial strain parallel to the interface to form a lattice-matched structure with the substrate. (b) Schematic of a relaxed thick film thicker than the *critical thickness*. A misfit dislocation (red) is shown at the epitaxial interface to relax the lattice strain. (Adapted from Fig. 7.12 in ref. [52])

laxation and effectively avoid misfit dislocations. This dissertation will focus on the lateral heterojunctions.

1.2 Scanning transmission electron microscopy

Scanning transmission electron microscopes (STEMs) [53–55] are, without a doubt, the ideal tool to study the atomic structures of 2-D materials, as they can provide atomic resolution images of the top and side projections. Conventional TEM, first built by Max Knoll and Ernst Ruska in 1932 [56], employs a parallel electron beam passing through the sample and projecting the magnified image onto a screen or a detector (Fig. 1.3). STEM was invented by von Ardenne six years later in 1938 [53] and was dramatically improved by Crewe et al. in the 1960s with the development of the cold field emission gun [54]. In contrast to conventional TEM, STEM focuses an electron beam as a fine probe which scans across the area of interest to form images of the sample (Fig. 1.3). STEM has numerous advantages comparing to conventional TEM. Most importantly, because no post-sample imaging lenses are needed in STEM, several detectors can be housed in the post-specimen area. Upon the selection of detectors, STEM can provide simultaneous bright field (BF), annular bright field (ABF), annular dark field (ADF), differential phase contrast (DPC) images, or electron energy loss spectroscopy (EELS) maps. These detectors collect the transmitted electrons that carry a variety of information from the sample. For example, the ABF detector preferentially collects an annulus in the bright center disk, displaying both heavy and light atoms in the image, while the ADF detector collects high-angle scattering electrons resulting in an image contrast proportional to the atomic number square. The EEL spectrometer analyzes the energy spectra from the inelastically scattered electrons and provides elemental information of the sample. Combining them all, a full description of the sample can be achieved from STEM imaging.

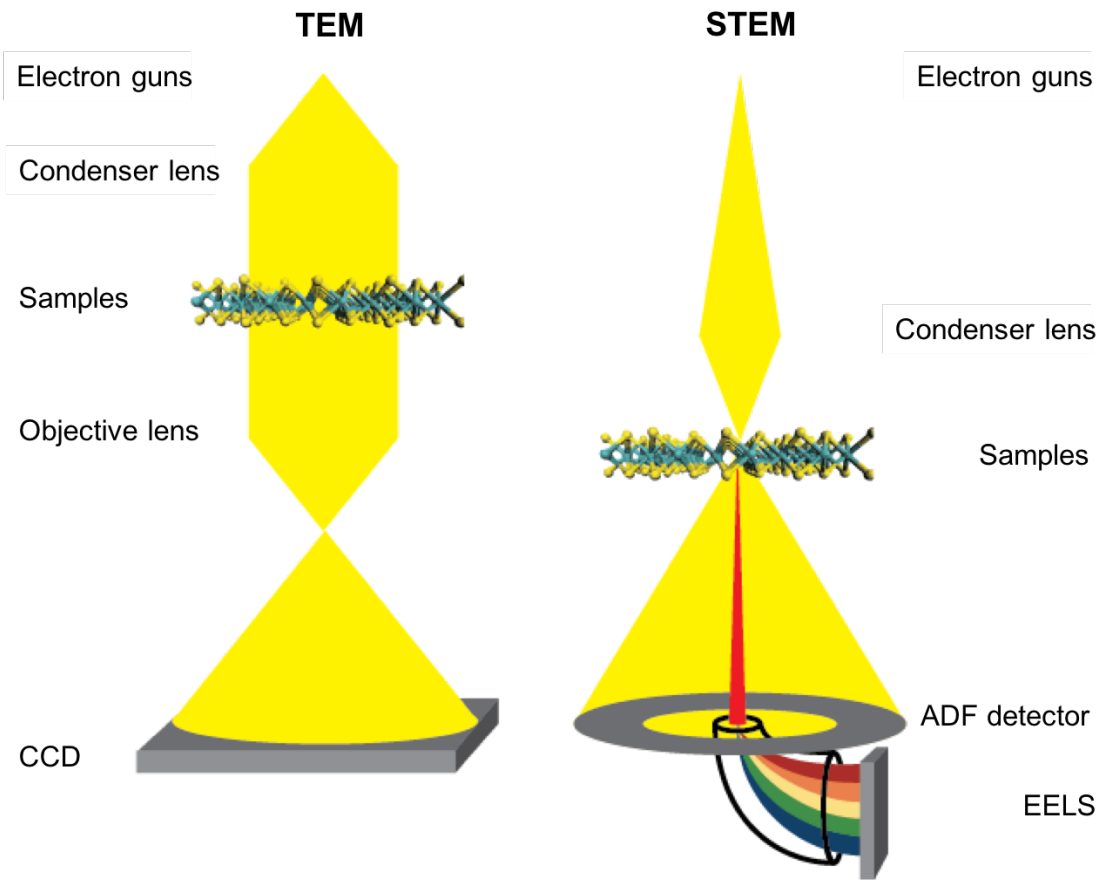

Figure 1.3: Diagrams of a TEM and a STEM. TEM uses a parallel beam to illuminate the entire sample region while STEM focuses the beam as a fine probe scanning across the sample. The electron gun, electromagnetic lenses, and detectors are shown on the schematic.

Accelerating voltages (kV)	Velocity of electrons ($m\,s^{-1}$)	Wavelength of electrons (Å)
60	1.3×10^8	0.049
80	1.5×10^8	0.042
100	1.6×10^8	0.037
120	1.8×10^8	0.033
200	2.1×10^8	0.025
300	2.3×10^8	0.019

Table 1.2: Velocities and wavelengths of electrons with different acceleration voltages (relativity considered).

1.2.1 STEM resolution

Before discussing detectors, the most important aspect in electron microscopy, and specifically in STEM, is typically the achievable resolution. Since a STEM focuses the electron beam into a fine probe that scans across the sample, the probe size directly defines the resolution of the STEM. The probe size is usually determined by the diffraction limit, where the spread of the probe can be approximated by $d_0 = 0.61\lambda/\alpha$ for incoherent imaging modes such as ADF ($d_0 = 1.22\lambda/\alpha$ for coherent modes) where d_0 is the probe size, λ is the wavelength of the electron beam, and α is the convergence angle. At different accelerating voltages (60-300 kV), the wavelengths of electrons are provided in Table 1.2. Although electrons used in STEM have pico-meter wavelength, the probe size is still limited by fundamental aberrations.

Geometric aberrations are introduced by the imperfect electromagnetic lenses in the electron microscopes, which distort the electron wave front and generate a phase shift on the specimen, leading to undesirable probe tails in STEM. Reducing these aberrations can improve the resolution of STEM with all accelerating beam voltages [57]. For decades, numerous efforts have been put into designing and building the aberration correctors [58–62]. Now, with the help of computers, operational aberration correctors have been developed and used in most high-resolution STEMs. One of the most sophisticated correctors is Nion's third- and fifth-order spherical aberration corrector, which can correct up to all 5th order geometric aberrations [58–60] and reach sub-Å resolution.

At low accelerating voltages (below 100 kV), the chromatic aberration dominates in a C_3 aberration-corrected electron microscope working at its optimized condition [63]. Although low voltages may help prevent the knock-on damages

of 2-D materials (graphene's knock-on damage threshold is 80 kV and MoS_2 is 60 kV), operating a microscope at lower voltages always leads to lower resolution due to the energy spread of the electron beam that causes the chromatic aberration. A sophisticated design of an electron source, such as the cold field emission gun (CFEG) in the Nion UltraSTEM possessing a small energy spread, can lead to higher resolution for low voltages. For other types of electron sources, a monochromator (energy filter) can contribute to a smaller energy spread of the electron beam, but decreases the electron beam current and leads to insufficient signals in ADF images. Along with additional difficulties to align the monochromator for STEM, using the monochromator for every sample examination is impractical. There is still room for commercial chromatic aberration correctors to contribute to higher resolution in STEM.

Besides aberrations, the probe can also be limited by the finite source size when the beam current is relatively high. Usually, measuring the coherent current defined as when the source size becomes comparable to the probe size for each source at different accelerating voltages helps to determine the optimal current. As an example, the CFEG's source size well below the coherent current condition (150-215 pA) can be ignored (D.A. Muller and L.F. Kourkoutis, Cornell University). Operating at the optimal beam current in electron microscopes is essential for high resolution in STEM.

1.2.2 How to interpret ADF-STEM images

ADF detectors are annular detectors coated with scintillators to convert electrons in vacuum to optical then electronic signals. Located at the back focal

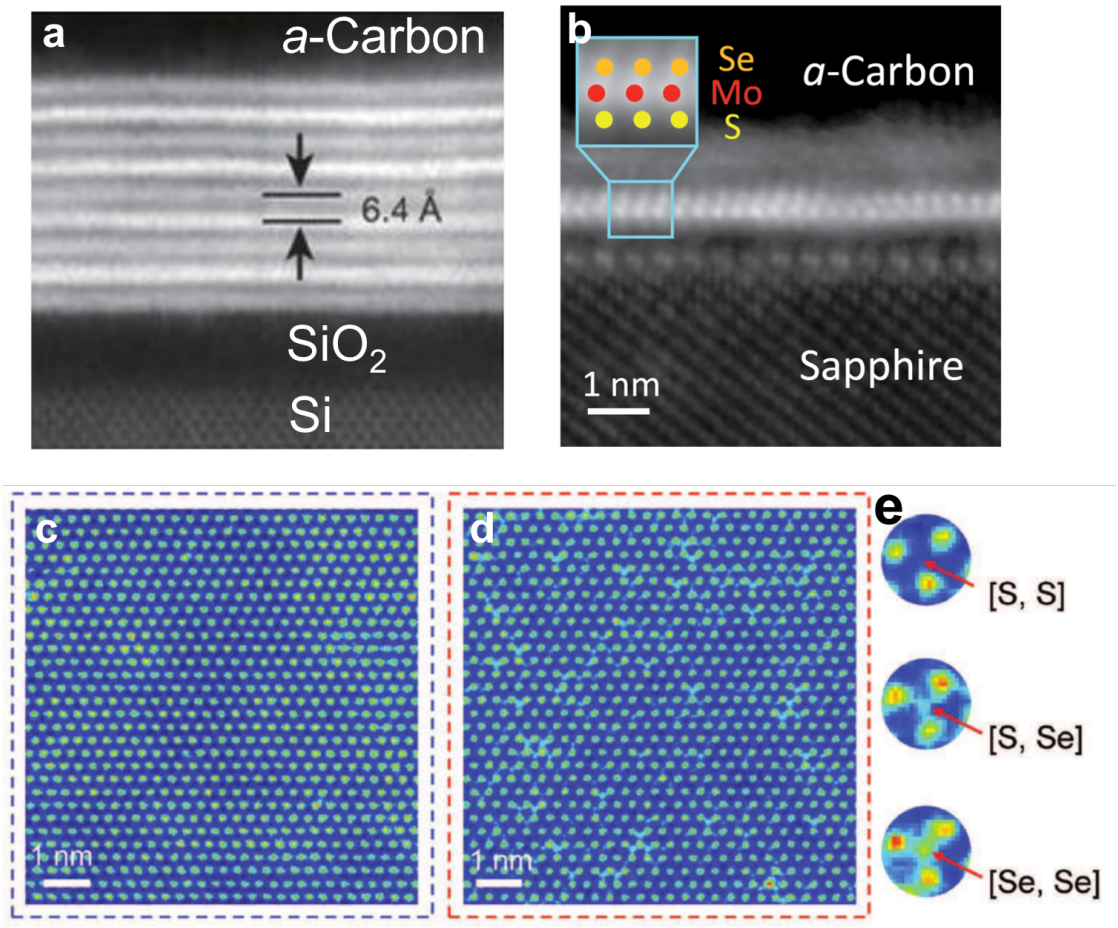

Figure 1.4: ADF-STEM images of cross-sectional and plan-view 2-D materials. (a) Cross-sectional image of a multi-stack heterojunction of MoS_2 and WS_2. The Mo and W atoms dominate the ADF contrast, so these two materials can be distinguished in this image (top to bottom, 1^{st},3^{rd},5^{th},7^{th},and 9^{th} layers are MoS_2, 2^{nd},4^{th},and 6^{th} layers are WS_2). [64] (b) Cross-sectional image of a Janus MoSSe, which has a similar lattice structure as MoS_2 while all sulfur atoms on the top are replaced by selenium atoms. [65] (c) Top-view image of WS_2 region in a WS_2-WSSe multi-junction sample. (d) Top-view image of WSSe region in the same sample where Se atoms dope WS_2 and form S-Se and Se-Se, which can be resolved by the ADF contrast (e). [66]

plane, the ADF detectors collect the electrons scattered elastically to an annulus around the primary beam (Fig. 1.3). The smallest angle of the annulus is called the inner collection angle, while the largest one is called the outer collection angle. Thus, the ADF intensity is directly determined by the integral of the electron counts between the inner and outer collection angles. Since the electron beam scans across the sample region, the image contrast can be interpreted as the direct indication of the electron scattering probabilities by individual atoms in the specimen.

The electrons scattered and deviated from their original trajectory are mainly elastically scattered electrons. At high scattering angles ($> 3\alpha$, where α is the convergence angle), these scattering events mainly from the nucleus, and can be described by the Rutherford scattering, whose scattering probability (i.e. the differential cross section) has an atomic number square dependence. Within this regime, the high angle ADF- (HAADF-) STEM image contrast of a thin sample is proportional to Z^2, where Z is the atomic number. However, for 2-D materials, usually a smaller inner angle ($1.5 \sim 3\alpha$) is used for stronger signals. In this regime, the nucleus surrounded by electron clouds can be described using a screened Coulomb potential, and thus leads to a Z^γ dependence of the ADF image intensity where $1.3 < \gamma < 2$ depending on the actual inner angle that was chosen.

ADF-STEM can be employed to determine the relative atomic numbers in cross-sectional 2-D specimens, as shown in Fig. 1.4 a where a nine-layer MoS_2/WS_2 vdW heterojunction has been made using a clean stacking approach [64]. As the tungsten atoms are heavier than molybdenum and sulfur, the four WS_2 layers appear brighter than the five MoS_2 layers. Each the layer shows as

a stripe due to the random crystal orientations of the 2-D films relative to their silicon substrates. Although atoms are not clearly resolved, their vdW interlayer distances were measured to be 6.4 Å, indicating no carbon contamination between layers. In addition, ADF-STEM can also provide atomic numbers in a Janus TMD structure [65], such as MoSSe shown in Fig. 1.4 b. This atomic resolution image resolves the selenium and sulfur atoms by contrast (Se is heavier than S) and confirms the Janus structure where all selenium atoms are placed on the top while sulfur atoms located at the bottom. To achieve this ADF-STEM image, the TMD flake needs to be aligned with the crystal orientation of its substrate. More details of the cross-sectional sample fabrication can be found in Appendix A.

In addition to cross-sectional images, uncovering the top-view structure of monolayer 2-D materials is also crucial, especially for in-plane heterojunctions (sample preparation methods provided in Appendix B). Top-view ADF-STEM of monolayer 2-D materials can determine the atomic number for each atom, such as single boron (or nitrogen) dopant in a monolayer graphene [67]. In TMD monolayers such as WS_2, although the tungsten atoms dominate the image contrast, ADF-STEM can still resolve the S-S, Se-S, and Se-Se doping sites (Fig. 1.4 c-e) [66].

1.2.3 EMPAD – a universal detector for STEM

The EMPAD is a high-speed, high-sensitivity, and high-dynamic-range detector designed at Cornell [68] usable for accelerating voltages from 20 to 300 kV (Fig. 1.5). As a universal detector in STEM, the EMPAD can acquire a full

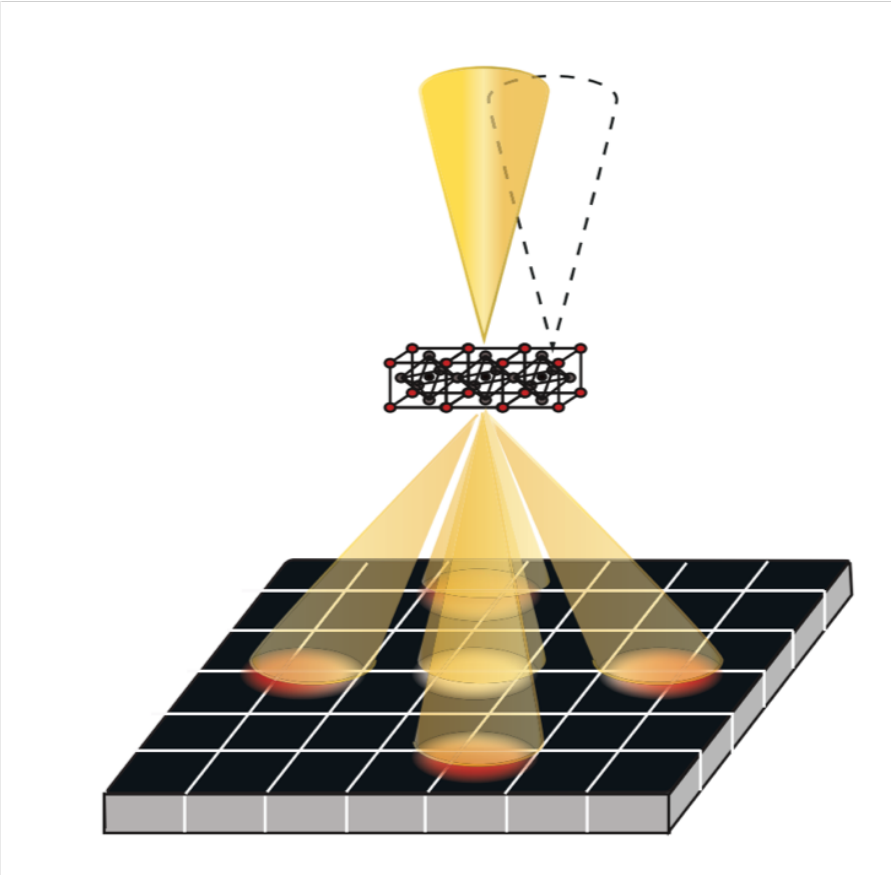

Figure 1.5: Schematic of the EMPAD. The EMPAD is a pixelated detector that collects diffraction patterns while the beam scan across the sample. (from ref. [68])

diffraction pattern at each scan position with a readout time of 0.86 ms/frame. Due to the high speed of the detector, a typical EMPAD 4-D dataset (x and y in real space and k_x and k_y in momentum space) at 256×256 scan points can be reached within minutes (depending on the acquisition time that was used). The fast speed is important for imaging 2-D materials, which is sensitive to the electron beam. Moreover, the single-electron sensitivity of the EMPAD allows for quantitative analysis of diffraction from a single atom [69] (Fig. 1.6 g), which is highly advantageous for studying 2-D materials. In addition, the EMPAD's high dynamic range enables collecting all transmitted electrons at all convergence angles with primary beam unsaturated and diffracted beams clearly resolved.

These advantages of the EMPAD allow for the extraction of multi-mode images from the EMPAD's 4-D dataset, including the integrated DPC (iDPC [70]) (Fig. 1.6 a), ADF (Fig. 1.6 b), ABF (Fig. 1.6 c), and BF (Fig. 1.6 d). Their line profiles (Fig. 1.6 f) provide direct comparison between these conventional imaging modes. In addition, the EMPAD also enables full-field ptychography that has achieved 0.39 Å resolution at 80 kV [71], and quantitative Lorentz-STEM [72] that maps magnetic and electric fields and provides 3-D reconstructions of polarization vortices [73]. In conclusion, EMPADs significantly enhance an electron microscope's capabilities and resolution limits, enabling STEM to become an even more powerful and versatile tool in materials science.

1.3 Dissertation overview

The materials and the characterization methods in this dissertation have been reviewed here. The body will discuss three projects using STEMs to uncover 2-D lateral heterojunction structures.

Chapter 2 will demonstrate the atomically sharp lateral heterojunctions of MoS_2 and WSe_2. Specifically, the lattice distortions at atomic scale will be elucidated. Atomic resolution ADF-STEM has been employed to display the lateral heterojunction atom by atom, uncovering the misfit dislocations at the heterointerfaces between MoS_2 and WSe_2 to relax the lattice strain due to the lattice mismatch. More importantly, these dislocations have been found very useful since they can grow the coherent MoS_2 channels embedded within WSe_2. From the ADF-STEM images and their strain analysis, the strong uniaxial strain in these embedded channels has been identified and studied, enabling electronic

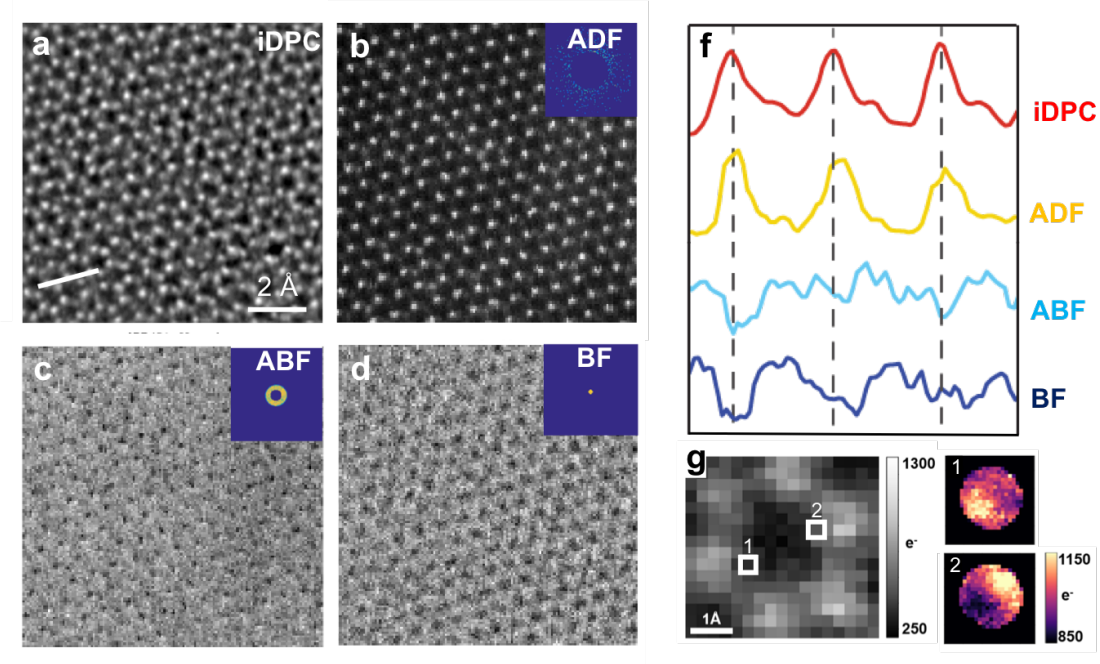

Figure 1.6: Atomic-resolution maps from EMPAD. (a-d) Images of a monolayer WS_2 are extracted from a single EMPAD 4-D dataset. (a) The iDPC (or iCoM) image was calculated by integrating the CoM of the diffraction pattern. (b) The ADF-STEM image with a 50 mrad inner collection angle and a 120 mrad outer collection angle. (c) The ABF-STEM image with 15(33) mrad inner(outer) collection angle. (d) The BF-STEM image was achieved by summing the diffraction intensity below 6 mrad. (f) shows the line profiles from (a-d), providing a direct comparison between different imaging modes. (g) displays the ADF-STEM image of a hexagonal ring and the corresponding diffraction patterns taken by the EMPAD. The contrast variation in the diffraction disk indicates a short-range field with features smaller than the probe (long-range field will cause the disk to shift).(g is from ref. [69])

band structure modulations. As the smallest patterns of dissimilar 2-D materials, these sub-nanometer channels can be potentially utilized in the ultimate electronic length scales.

Chapter 3 changes focus to the lateral heterojunctions of WS_2 and WSe_2. Due to the large length scales of the multi-junction region, atomic resolution approaches become impractical. The accurate and efficient strain mapping ap-

proach by the EMPAD will be discussed in this chapter. Moreover, a novel method to map the out-of-plane ripples in 2-D materials has also been developed using the same detector. These techniques have revealed the lattice distortions at these 2-D lateral heterojunctions, and thus, for the first time, uncovered the unique strain relaxation mechanism in 2-D lateral heterojunctions.

After discussing semiconductor lateral heterojunctions, Chapter 4 will focus on metal-semiconductor interconnects – the graphene-MoS_2 lateral heterojunctions. In order to make them atomically thin, MoS_2 as the transistor materials are laterally connected to monolayer graphene. Due to the dissimilarity of the lattice structures between MoS_2 and graphene, rather than epitaxial interfaces, they form narrow vdW junctions along the lateral heterointerfaces. In this work, several conventional electron microscopy techniques including dark field TEM, ADF-STEM, and EELS have been employed.

The final chapter contains a summary of this dissertation and potential future directions.

In the appendix, experimental details about sample preparation and data processing will be provided.

CHAPTER 2

ATOMICALLY SHARP MOS_2–WSE_2 LATERAL HETEROJUNCTIONS

My collaborators, Prof. Lain-Jong Li's team, reported the growth of atomically sharp MoS_2-WSe_2 [39]. This work attracted our attention and initiated our collaboration to study the atomic structures at the interfaces between MoS_2 and WSe_2. From their samples, we identified the growth of sub-nanometer MoS_2 channels embedded in WSe_2 monolayers the most personally significant finding of my Ph.D. The forth part of this chapter (2.4) was adapted from our paper published in Nature Materials: Y. Han, M.-Y. Li, G.-S. Jung, et al., "Sub-nanometre channels embedded in two-dimensional materials", Nature Materials 17, 129-133 (2018)

2.1 Introduction

The discovery of 2-D semiconducting TMDs has naturally led to the creation of semiconducting devices, such as transistors, logic gates, diodes, and ultimately light emitting devices (LEDs). As there is a large selection of TMD properties, it is very natural to consider the usage of monolayer *n* and *p*-type materials, with appropriate band alignments, to create atomically thin *p*-*n* junctions. Early works manually transferred MoS_2 (*n*) and WSe_2 (*p*) to form these micron scale devices [74,75], but the imperfect junction between the two materials is not ideal for 2-D devices. In contrast, the chemical synthesis can both address the issue of scale as well as atomically sharp interface between the 2-D semiconductors to form an epitaxial in-plane *p*-*n* junction, as previously reported [39]. As the length scales decrease, the atomic structures at the lateral heterointerfaces will dominate the local properties and thus affect the device performance. As we noted in the previous chapter (Table 1.1), the MoS_2 and

WSe_2 have a 4.5% lattice mismatch, indicating either coherent interfaces with uniaxial strain or periodic misfit dislocations at the interface to relax the lattice strain, the result of which can drastically affect the ultimate device performance.

This chapter will first describe the broad MoS_2 and WSe_2 lateral heterojunctions, which possess periodic interfacial dislocations that are generally expected to introduce mid-gap states and degrade the device performance [28, 29]. Although misfit dislocations are undesirable, dislocations as catalysts are essential in the growth approach we developed to fabricate narrow MoS_2 channels. In contrast to the broad MoS_2-WSe_2 lateral heterojunctions, which ultimately generate misfit dislocations to release the lattice strain, thin channels can sustain large strains without relaxation and hence access a wider range of electronic band structures.

2.2 Sample growth and fabrication

To achieve WSe_2-MoS_2 epitaxial lateral heterojunctions, the WSe_2 monolayers were first grown on sapphire substrates, using a solid-precursor CVD method [19], where the precursors (WO_3 and Se) are carried by hydrogen and argon gases in a heated furnace, and then deposited on the target substrates placed on the downstream side. After cooling, the samples were taken out of the WSe_2 furnace and placed in another specific one used only for MoS_2, and then MoS_2 monolayers were grown with MO_3 and S precursors. Most MoS_2 starts to grew from the WSe_2 edges and form epitaxial interfaces. This approach, called two-pot growth, effectively avoids any precursor residues or contaminants that cause doping effects, resulting in atomically sharp interfaces. Meanwhile, the

sub-nanometer MoS_2 channels are generated during the same growth process under a favorable sulfur precursor concentration. More growth details can be found in references [39, 48].

After the growth, a polymer transfer approach was employed to release the 2-D film from the substrate. The sample was coated with polymethyl methacrylate (PMMA). Hydrogen fluoride (HF) solution was used to separate the film from the substrate. The film was transferred to de-ionized (DI) water to clean off the HF, and then was scooped by a holey carbon TEM grid. After air-drying, the polymer was removed by vacuum annealing, leaving the suspended 2-D film over the holes for TEM study. (More details of the TEM sample preparation can be found in Appendix B.1)

2.3 Broad MoS_2–WSe_2 lateral heterojunctions

The atomic structures at the epitaxial interfaces of broad lateral heterojunctions are essential to their properties and applications. Fig. 2.1 a [39] shows an optical image of a micrometer-sized MoS_2-WSe_2 lateral heterojunction on sapphire substrate, where the two materials show slight color difference. Atomic resolution ADF-STEM, whose contrast is proportional to the atomic number square, provides detailed atomic structures at the hetero-interface. The difference in the atomic number between tungsten and molybdenum offers high contrast between the WSe_2 and MoS_2 regions, as shown in Fig. 2.1 b-d (W atoms are brighter than Mo) [76]. Near the abrupt interface, only a few interstitial tungsten atoms were observed on the MoS_2 side. Other than that, most areas in the 2-D lateral heterojunction preserve their original chemical bonds and lattice

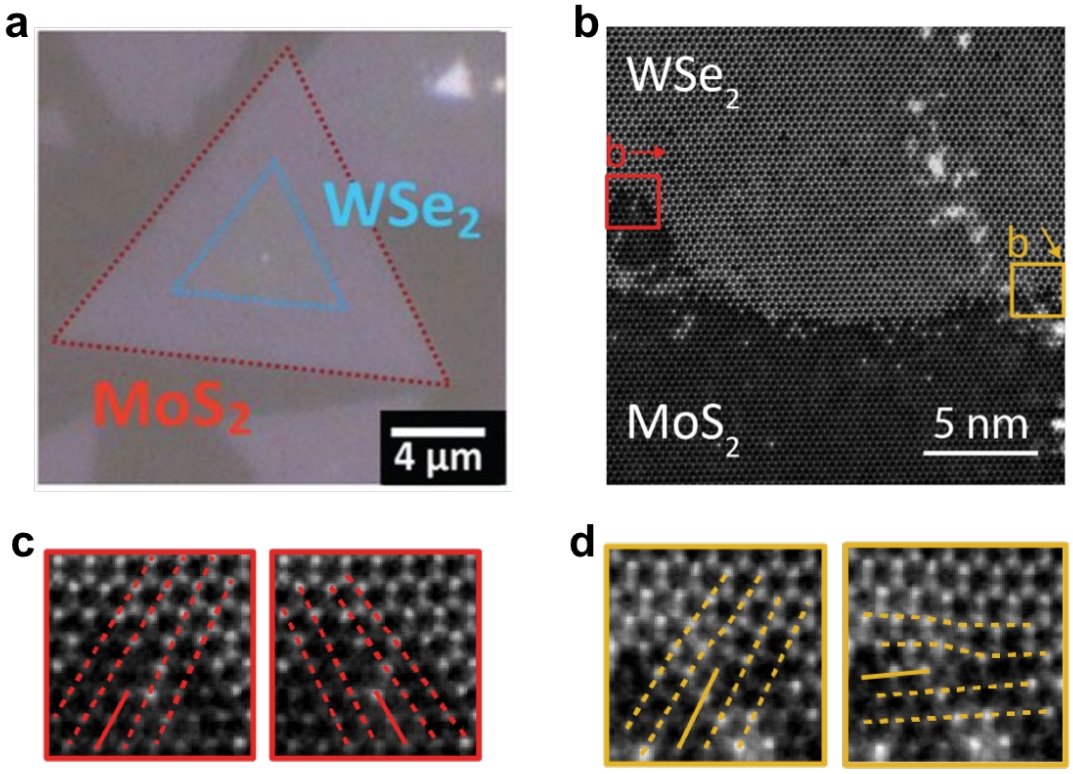

Figure 2.1: Atomically sharp lateral heterojunctions. (a) Optical image of the MoS_2-WSe_2 lateral heterojunctions [39]. Both MoS_2 and WSe_2 are at micrometer scale. (b) Atomically resolved ADF-STEM image at the interface with two misfit dislocations sectioned off. The orientations of two different Burger's vectors are indicated by arrows in red (0° to the interface) and yellow (60° to the interface), respectively. (c,d) Magnified images with labelled atomic planes (dashed lines). The extra atomic planes that create the misfits are indicated by solid lines. ((b-d) are from ref. [76])

structures.

As we know, these two materials, MoS_2 and WSe_2, have a 4.5% lattice mismatch, with WSe_2 being larger. Although such small amount of lattice difference cannot be easily distinguished in the ADF-STEM image (Fig. 2.1 b), it is large enough to generate a number of periodic misfit dislocations at the epitaxial interfaces. By examining the ADF-STEM image very carefully, two misfit

dislocations have been identified at the epitaxial interface. In Fig. 2.1 b, these two misfit dislocations are sectioned off with their Burger's vectors displayed on top. Although the Burger's vectors point to different directions, both of them still contribute to relax the lattice strain since they introduce additional atomic lines in the MoS_2 side (solid lines in Fig. 2.1 b and c).

2.4 Narrow MoS_2 channels in WSe_2 monolayers

While MoS_2-WSe_2 lateral heterojunctions achieved the thinnest possible *p-n* junctions [39], precise nanoscale control over the lateral dimensions are also necessary. This part will demonstrate the direct synthesis of sub-nanometer-wide 1-D MoS_2 channels embedded within WSe_2 monolayers, using a dislocation catalyzed approach. The 1-D channels have edges free of misfit dislocations and dangling bonds, forming a coherent interface with the embedding 2-D matrix. Periodic dislocation arrays produce 2-D superlattices of coherent MoS_2 1-D channels in WSe_2. These quantum confined channels and superlattices can be applied for the engineering of future atomic circuitry at the ultimate length scale.

2.4.1 Synthesis of 1-D channels

We start with a broad lateral heterostructure (Fig. 2.1). Then, the growth precursors were introduced and provided a high chemical potential of the channel material. The high reactivity in the core of the misfit dislocations allows the channel atoms (Mo and S) to be inserted into the dislocation core, thus pushing

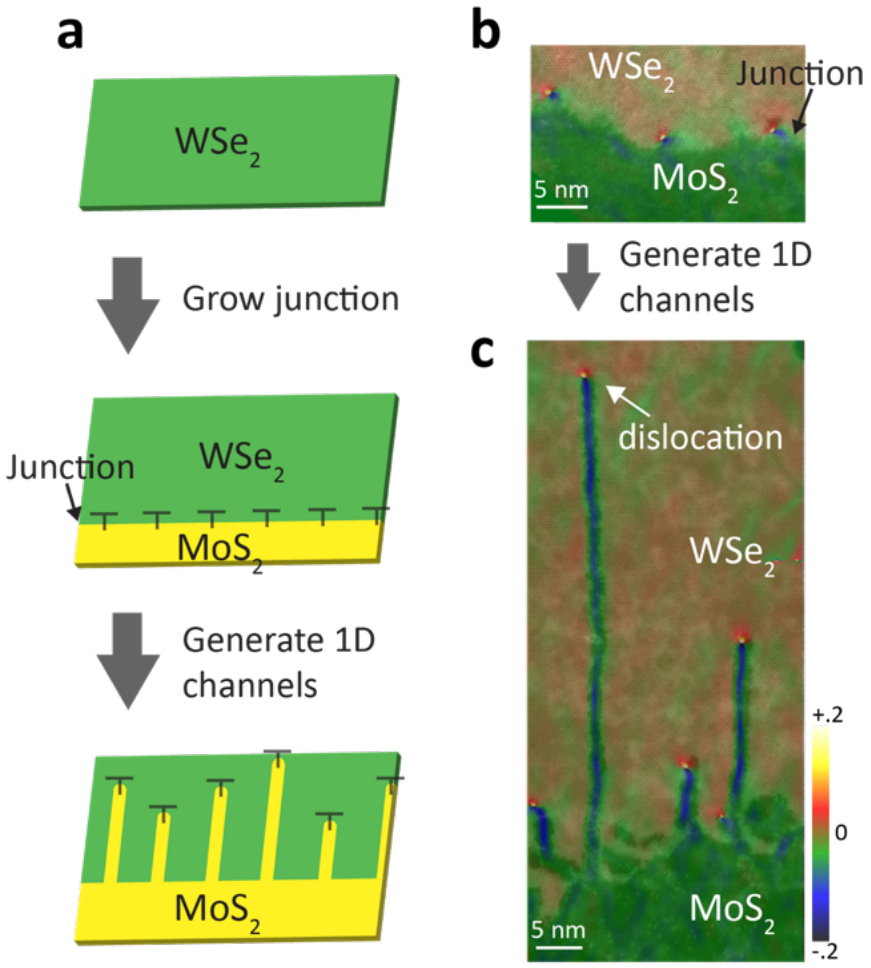

Figure 2.2: Formation of 1-D channels. (a) Schematic of the patterning process guided by misfit dislocations (marked as "T") at the MoS_2-WSe_2 lateral heterojunction. (b,c) Atomic resolution ADF-STEM images overlaid with its ε_{xx} strain maps (see Fig. 2.3 for more details) identifying the periodic dislocations at the interface of MoS_2 and WSe_2 (b) and the 1-D channels created by chemically-driven migration of the interfacial dislocations as additional S and Mo atoms are added (c). Strain maps refer to the WSe_2 lattice.

the dislocations away from the original interface, forming 1-D MoS_2 channels in a trail behind the advancing core, as shown in Fig. 2.2. The dislocation-catalyzed growth is essentially the flat analog of the semiconductor nanowires whose growth from seeded catalysts has played an important role in semiconductor nanoscience.

2.4.2 Uniaxial strain in 1-D channels

ADF-STEM imaging shows that the epitaxial interface between the body of the channel and the host matrix is coherently connected (Fig. 2.3 a). Meanwhile, a pentagon-heptagon (5|7) dislocation (heptagon pointing up) is found at the terminus of all 1-D channels (Fig. 2.3 b). The as-grown heterostructures of the TMDs must contain strain, due to the bond mismatch to create an epitaxial interface. Applying a geometric phase analysis (GPA) [77] to the ADF-STEM image in Fig. 2.3 a, we are able to elucidate the strain distribution in and around this 1-D channel in its 2-D matrix, as plotted in Fig. 2.3 c-f. For GPA, the WSe_2 lattice parameter was chosen as the reference or zero strain. More details about the GPA method can be found in Appendix C. Along the x-axis, there is significant difference in the strain map between the 2-D WSe_2 and 1-D MoS_2 channels, arising mainly from the lattice mismatch (Fig. 2.3 c). In contrast, the y-axis strain map reveals that MoS_2 channels have an identical lattice spacing with the host WSe_2 (Fig. 2.3 d), indicating a high uniaxial tensile strain along the y-direction. Therefore, the newly synthesized 1-D channel maintains coherency with the WSe_2 matrix and is strain accommodated, which effectively avoids the generation of misfit dislocations along the channel. The shear map and rotation map (Fig. 2.3 e and f) display the position and orientation of the dislocations as dipole fields, confirming all dislocations have the same orientation and migrate upwards (i.e. away from the original hetero-interface).

Fig. 2.3 g shows the ADF-STEM image and corresponding ε_{xx} strain map of a MoS_2 1-D channel that was formed from an intrinsic catalyst dislocation migrating in the direction of the heptagon. This indicates that the growth of the 1-D channels is not limited to the interfacial misfit dislocations at the heterostructure

interface of the two 2-D materials. They can also be generated from intrinsic 5|7 dislocations implanted within the WSe_2 film. This specific isolated 1-D channel is 70 nm in length and 1.5 nm in width, surrounded by monolayer WSe_2 on all sides, showing a high-aspect-ratio of about 47:1 (length to width).

2.4.3 Statistics of 1-D channels

The dislocation movement out of its slip plane (*climb* [34]) also occurs in a 3-D epitaxial interface, due to the diffusion of vacancies or interstitial atoms. In the bulk, this typically does not produce any major effects. In contrast, misfit dislocations in 2-D materials can directly take (release) atoms from (to) the environment, suggesting persistent climbs that can be used to pattern 1-D channels by controlling the precursors and growth time. Statistically, 76% of dislocations tend to migrate and form 1-D channels under our optimized growth conditions. More than 90% of the 1-D channels have widths that are less than 2 nm, confirming the high accuracy of the dislocation-guided patterning process (Fig. 2.4 a). A histogram of channel length is shown in Fig. 2.4 b, of which the longest channels reached 80 nm. The length of the 1-D channels was strongly correlated with the precursor ratio (S:Mo) and the growth time, suggesting these are two key underlying control parameters. However, there is a limit to how long the MoS_2 channels can be grown. As the surrounding MoS_2 layer continues to grow, the channel growth ultimately becomes unstable – the 1-D channels have possibility to branch repeatedly and recursively, leading to tree-like structures that eventually consume the host material. The channel branching will be discussed in 2.4.5.

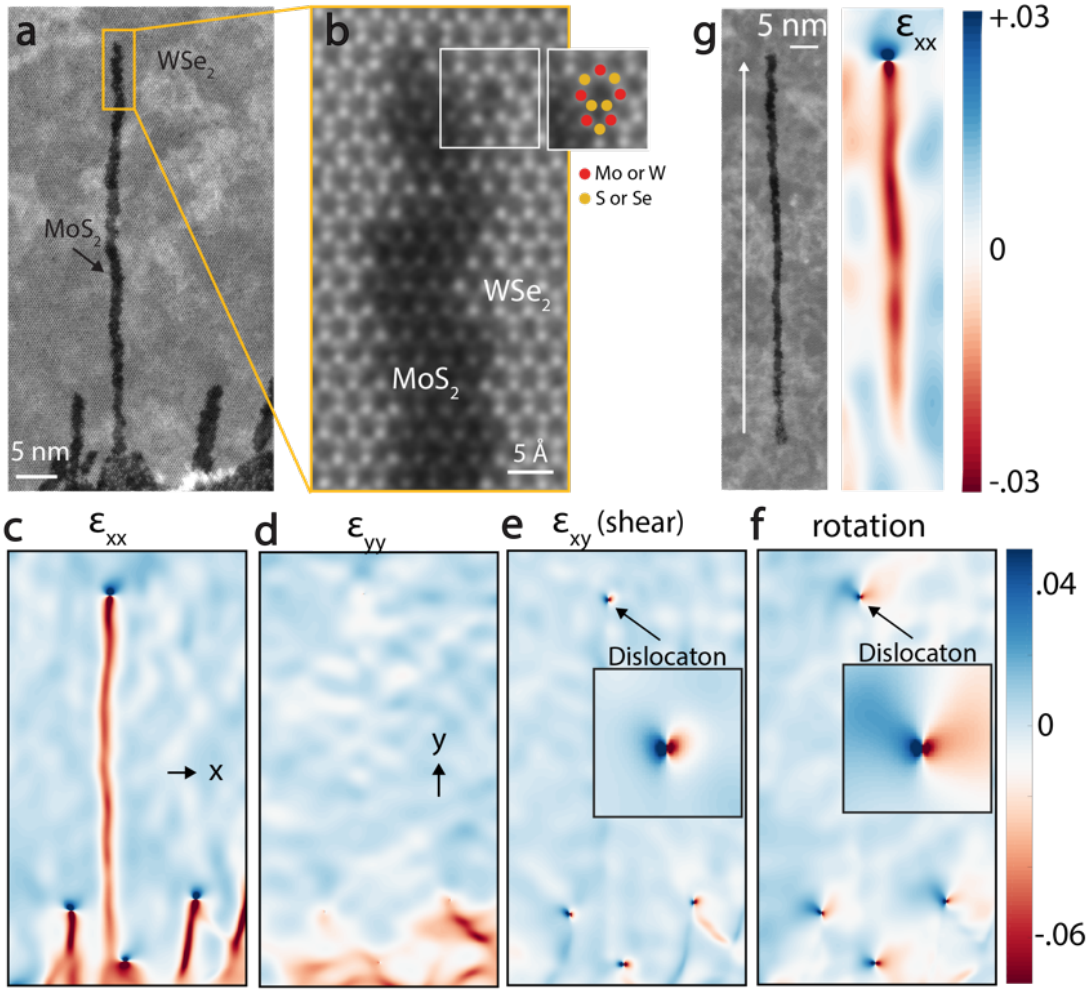

Figure 2.3: Strain maps of the 1-D channels. (a,b) ADF-STEM image of MoS_2 1-D channels embedded within WSe_2. The channel ends with the 5|7 dislocation (white box in (b)). The same section is shown to the right with the atoms labeled. (c,d) GPA of the 1-D MoS_2 in (a) with uniaxial strain components ε_{xx} (c) and ε_{yy} (d). All the strain is in reference to the WSe_2 lattice. The ε_{xx} clearly distinguishes the two lattices mainly due to the lattice mismatch, while the ε_{yy} indicates a high uniaxial tensile strain in the 1-D MoS_2 which is lattice mismatched from the WSe_2. (e,f) display the shear strain and the rotation map (in radians) indicating the position and orientation of the dislocations. (g) ADF-STEM image and its ε_{xx} strain map of a MoS_2 1-D channel formed from an intrinsic 5|7 dislocation in WSe_2, which matches the results found in channels arising from the heterojunction interface.

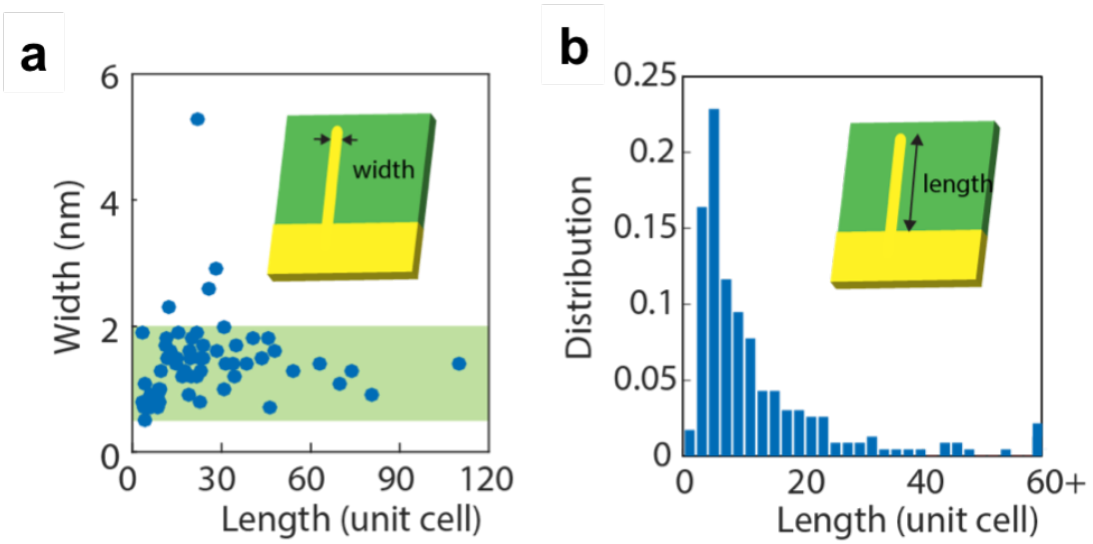

Figure 2.4: Statistics of 1-D channels. (a) The scatter plot of the channel width according to their length shows that more than 90% of the channels have widths less than 2 nm. (b) The length distribution of the 1-D channels displays an abrupt drop below 2 nm, suggesting that most 1-D channels tend to grow once the catalyst dislocations start to migrate. Our statistics of the width and length are from ~ 150 1-D MoS_2 channels.

2.4.4 1-D channel superlattices

The nature of the 1-D growth can be used to create lateral 1-D superlattices in 2-D materials starting from a periodic dislocation chain, as illustrated in Fig. 2.5 a. The most common structures with periodic dislocations are the grain boundaries of 2-D materials [26,28,29,78]. At a typical low-angle WSe_2 grain boundary, where two grains with small rotation angles connect laterally to form a classic low-angle tilt boundary, the periodic arrays of 5|7 dislocation cores line up with a spacing proportional to b/θ. Here, b is the Burger's vector and θ is the tilt angle between the two grains, suggesting grain boundary tilt angle can be used to control the 1-D channel spacing. In theory, the dislocations are most stable when they lie vertically above one another with equal spacing [34]. To attain the

lowest energy over large scales, the dislocations at the originally curved grain boundary (blue dashed line in Fig. 2.5 b) migrate with an angle of 30° to the left (or to the right) of the heptagon direction to form a straight grain boundary.

The magnified ADF-STEM image (Fig. 2.5 c) shows a region where all catalyst dislocations migrate 30° to the left forming ~1 nm nanowire arrays with sub-nanometer spacing. Fig. 2.5 d to g present the strain maps of Fig. 2.5 c, indicating that dislocations keep their periodicity and orientations after the translation, and the right-side lattice orientation is inherited. We note that in Fig. 2.5 c, short branches appear also on the right side of the original grain boundary, but they have no dislocations at the ends. This can be understood as arising from individual dislocation wandering before they are propelled towards the left by other dislocations, suggesting a strong collective interaction between dislocations that can be used to control the patterning of 1-D superlattices.

2.4.5 1-D channel branching

As mentioned in 2.4.3, the lengths of the 1-D channels are limited by the stability of the dislocations. Higher sulfur concentration or a longer growth time induces instability of the catalyst dislocations, where they can split into two partial dislocations, and essentially cause the 1-D channel to branch (Fig. 2.6 a-c). GPA maps show that the partial dislocations have different orientations (Fig. 2.6 d), allowing them to migrate separately. However, the sum of the Burger's vectors of the partial dislocations equals to that of the original catalyst dislocation before splitting. The Burger's vector for each dislocation is conserved during

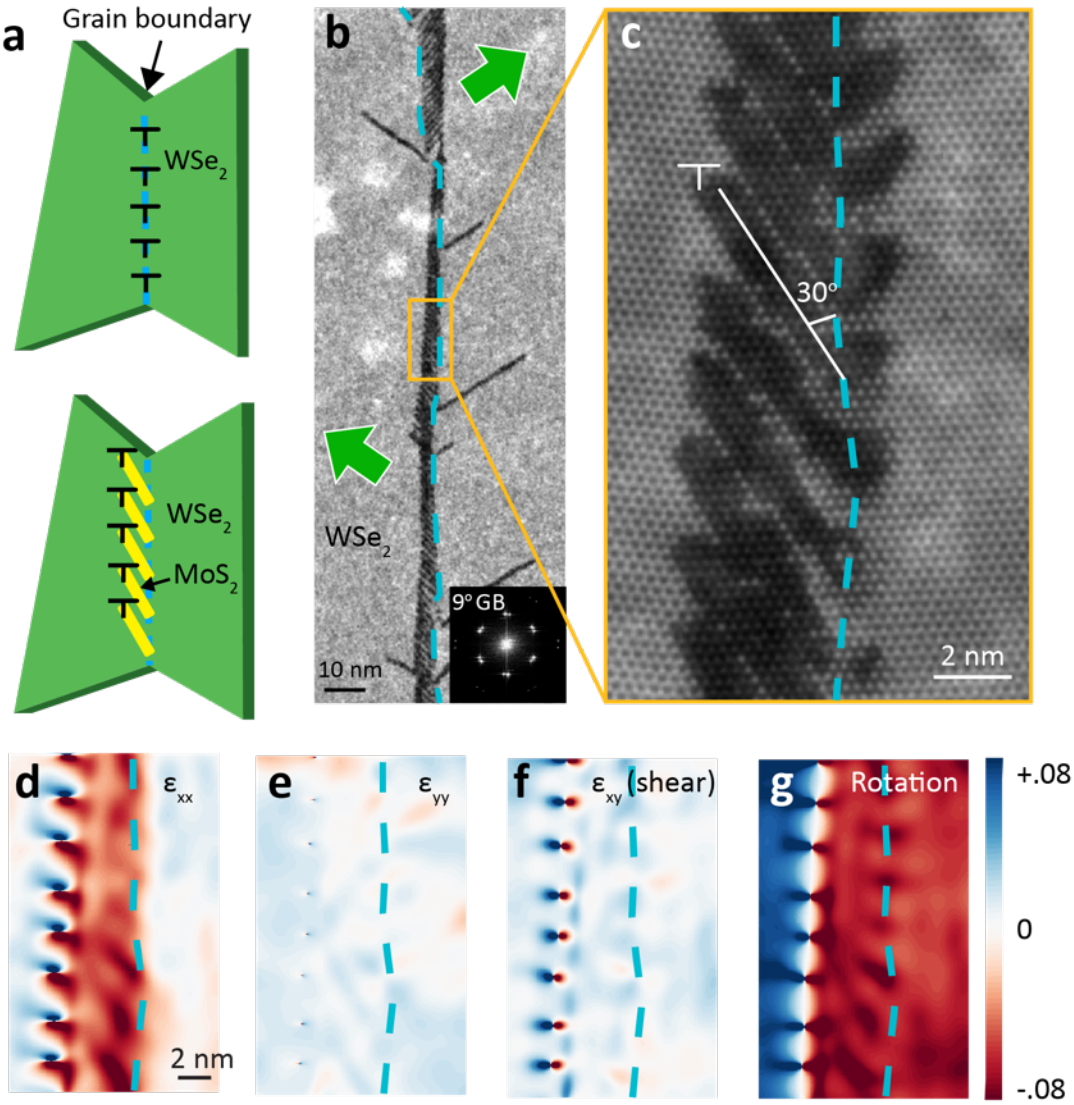

Figure 2.5: 1-D channel superlattices (a) Schematic of the superlattice formation where the top (bottom) panel depicts the grain boundary before (after) the patterning process. (b) ADF-STEM image of a superlattice grown from the periodic dislocations at the WSe_2 grain boundary with 9° rotation (2 nm spacing between dislocations). All blue dashed lines indicate the position of the original curved grain boundary. The dislocations migrate in different directions (indicated by the green arrows), thus forming a shifted but straight grain boundary. (c) Magnified ADF-STEM image with one of the identical dislocations marked by a "T". (d-g) GPA of (c) showing that dislocations preserve their periodicity and orientations during the migration.

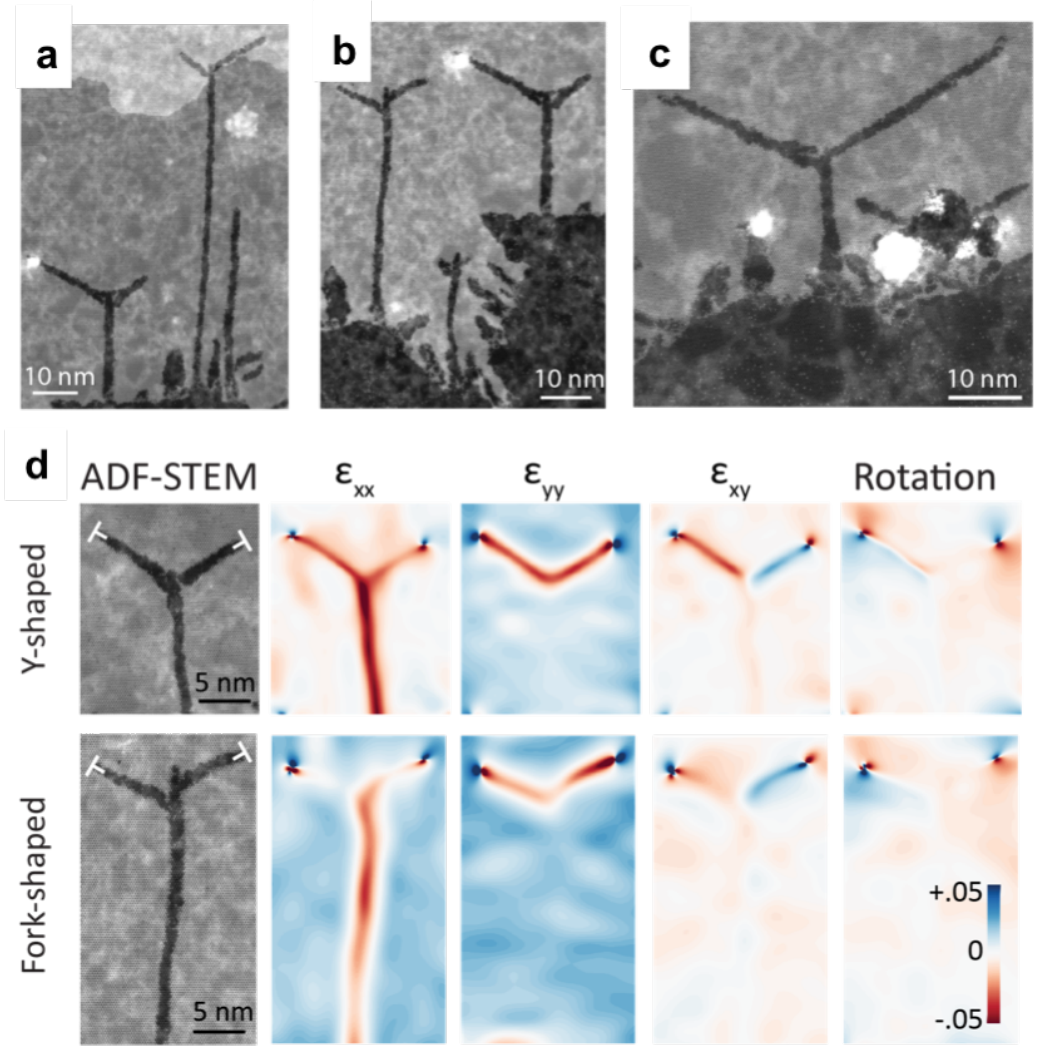

Figure 2.6: 1-D channel branching. (a-c) ADF-STEM images showing the catalyst dislocations split into two partial dislocations and form branches. The instability at the hetero-interfaces also cause some WSe_2 to be replaced by MoS_2, leading to a rough lateral heterojunction. (d) ADF-STEM images and their corresponding strain maps of the Y-shaped and fork-shaped junctions. The orientations of the partial dislocations are marked as "T" on the ADF images, indicating a total Burger's vector that equals to the Burger's vector of the original dislocation.

the entire splitting process.

2.5 Conclusion

To summarize, the atomically sharp lateral heterojunctions grown using a two-pot CVD approach possess micrometer scale. Due to the lattice mismatch between these two materials (MoS_2 and WSe_2), the lateral hetero-interfaces are decorated by periodic misfit dislocations (5|7 member rings) to relax the lattice strain caused by the lattice mismatch.

The misfit dislocations as highly reactive centers can perform as catalysts to initiate the growth of sub-nanometer 1-D MoS_2 channels embedded within the 2-D WSe_2 matrix. The embedded MoS_2 channels possess atomically coherent sidewalls free of misfit dislocations and dangling bonds. The strain accommodation and coherency of these 1-D channels result in a strong uniaxial strain, which can be engineered upon the selection of the 2-D matrix materials. As a summary of our growth strategy to produce these dislocation-free 1-D channels, a general set of search criteria for other 2-D materials will be listed:

- First, candidate materials need a source of dislocations such as low-angle grain boundary or lattice mismatched hetero-interface.
- Secondly, while the dislocations allow for an easier insertion and exchange of atoms, the substitutions need to be energetically favorable (e.g. S for Se).
- Third, the lattice mismatch is also required for the dislocation to climb. Combinations of materials that have little lattice mismatch, such as MoS_2 and WS_2, will not form 1-D channels due to the lack of a lattice mismatch.

CHAPTER 3

WS_2–WSE_2 LATERAL HETEROJUNCTIONS

This chapter is adjusted from our paper: Y. Han, et al., "Strain Mapping of Two-Dimensional Heterostructures with Sub-Picometer Precision" arXiv: 1801.08053. This work exploits the EMPAD, a newly developed detector from our group [68]. The heterojunction samples are provided by Prof. Jiwoong Park's team. [49]

3.1 Introduction

In order to achieve optimal electronic and optoelectronic properties, the 2-D lateral heterostructures should avoid undesirable misfit dislocations. Taking inspiration from bulk epitaxy [34], growing thin films below their *critical thickness* can effectively reduce the dislocation density at the hetero-interfaces. As discussed in the former chapter, the narrow channels whose widths (less than 2 nm) are always below the *critical thickness*, form coherent interfaces that are free of misfit dislocations. In this chapter, the WS_2-WSe_2 lateral heterojunctions possess different widths (~500 nm and ~100 nm). Studying the atomic structures of the WS_2-WSe_2 lateral heterojunctions can provide an estimate of their *critical thickness* and uncover the strain relaxation mechanism.

Since the regions of interest in the WS_2-WSe_2 junction samples usually span more than a few hundred nanometers, atomic resolution techniques, such as ADF-STEM and GPA which have a field-of-view that is limited to a few tens of nanometers, become impractical for these multi-junctions. Conversely, nanobeam diffraction (NBD) combined STEM [79–83] effectively decouples the spatial resolution from the strain mapping precision, allowing for

high-precision strain measurements across a larger sample area. However, this approach on 2-D materials has historically been limited by the speed and dynamic range of the existing detectors, as 2-D materials are sensitive to the electron beam and are weak scatterers. To overcome these issues, we developed a method to map the strain and identify dislocations in 2-D crystals using an EMPAD [68] designed at Cornell.

3.2 NBD with EMPAD

The EMPAD has high-speed, high dynamic range, and high sensitivity (Fig. 3.1 a). This allows the scanning NBD to be achieved within minutes with no noticeable damage to 2-D samples, ultimately providing sub-picometer precision strain mapping over length scales, ranging from angstroms to many micrometers. The EMPAD operates at a range of accelerating voltages from 20 to 300 kV (Our experiment was conducted at 80 kV, and this is typical for 2-D materials). Moreover, the EMPADs high sensitivity and dynamic range enables collection of all transmitted electrons at small convergence angles with the primary beam unsaturated and diffracted beams clearly resolved (Fig. 3.1 b), as demonstrated by integrating the center beam (and one diffracted spot) to plot the virtual bright field (and dark field) images, as shown in Fig. 3.1 c and d.

3.3 Broad WS_2–WSe_2 lateral heterostructures

The epitaxial WS_2-WSe_2 heterojunctions were synthesized through metal-organic chemical vapor deposition (MOCVD) [22,49] on SiO_2 substrates. Due to

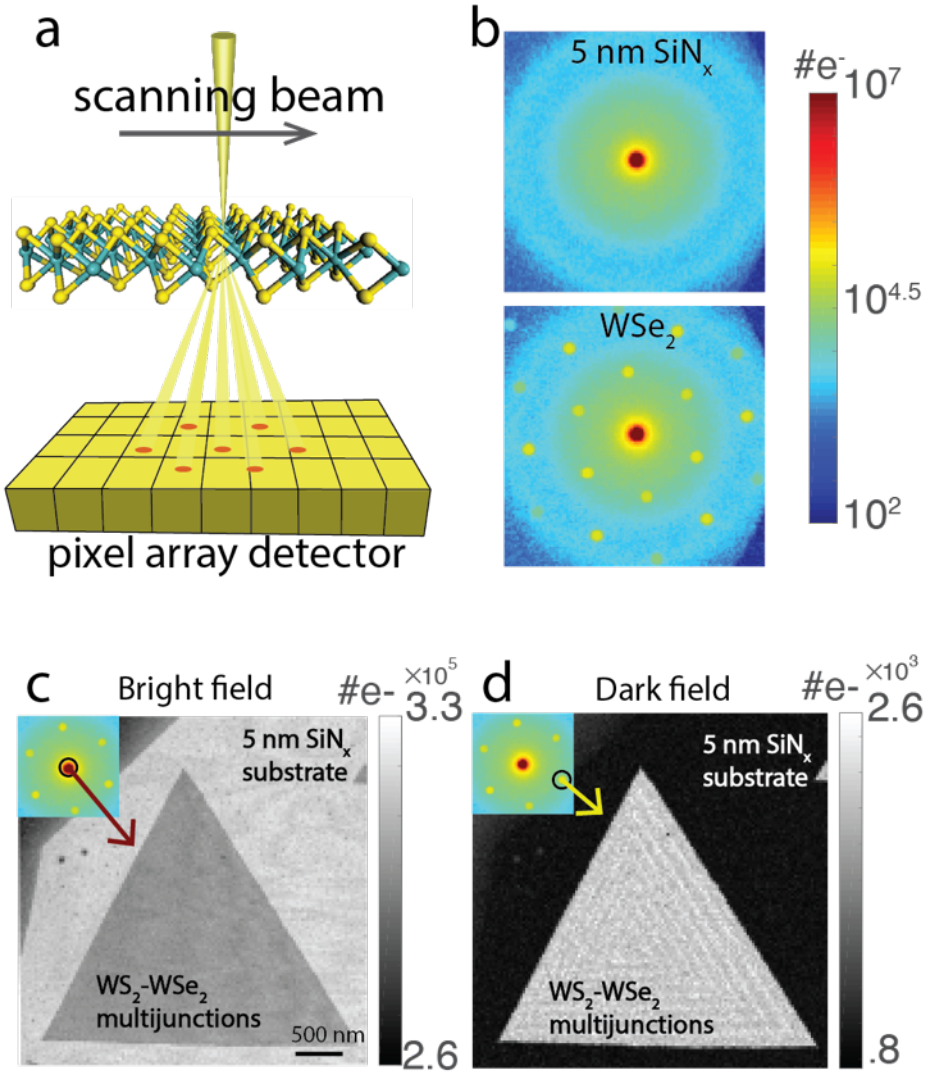

Figure 3.1: Imaging 2-D materials with an EMPAD. (a) Schematic of the EMPAD operation, where a full diffraction pattern, including the unsaturated primary beam, is recorded at each scan position. (b) Diffraction images taken by EMPAD. The top panel shows the diffraction image of a 5 nm SiN_x film, while the bottom panel displays the diffraction pattern of a WSe_2 monolayer located on the 5 nm SiN_x film. (c,d) show the virtual bright field and filtered dark field images obtained by integrating the central and the labeled diffracted beam, respectively, as indicated on their top left sections.

the one-pot approach that switches precursors *in-situ*, the WS_2 and WSe_2 merge with graded interface. In the broad lateral heterojunctions, the widths of both WS_2 and WSe_2 films are about 500 nm, still beyond their *critical thickness*. As a result, mostly relaxed lateral heterojunctions with misfit dislocations forming at the junction interfaces are expected.

3.3.1 Sub-picometer lattice constant mapping

From the EMPAD's 4-D dataset of the broad WS_2-WSe_2 lateral heterojunction, we extracted the ADF-STEM signal (Fig. 3.2 a) by integrating the diffraction patterns masked by a virtual ADF detector. The ADF-STEM image provides the triangle outline of the flake, but little contrast difference between WS_2 and WSe_2, as the heavy tungsten atoms dominate the contrast.

In contrast, the lattice constant map (Fig. 3.2 b) calculated by measuring shifts in the reciprocal lattice vectors clearly distinguishes the two materials, which contain nanometer-sharp interfaces (inset of Fig. 3.2 b). From a histogram of lattice constant measurement (Fig. 3.2 c), we extracted the mean values as the statistically averaged lattice constant for WS_2 (3.182 ± 0.0005Å) and WSe_2 (3.282 ± 0.001Å), indicating a 3.1% lattice mismatch (fully relaxed films have 4.5% lattice mismatch). The histogram (inset of Fig. 3.2 c) from a flat region (gray box in Fig. 3.2 b) indicates this method has a precision higher than 0.3 pm, with local sample distortions placing an upper limit on the spread. The sub-picometer precision of the lattice constant mapping relies on high angular resolution when we measure the centers of the diffraction spots. For 2-D materials in this project, we used the center of mass (CoM) to identify the centers, which is an efficient

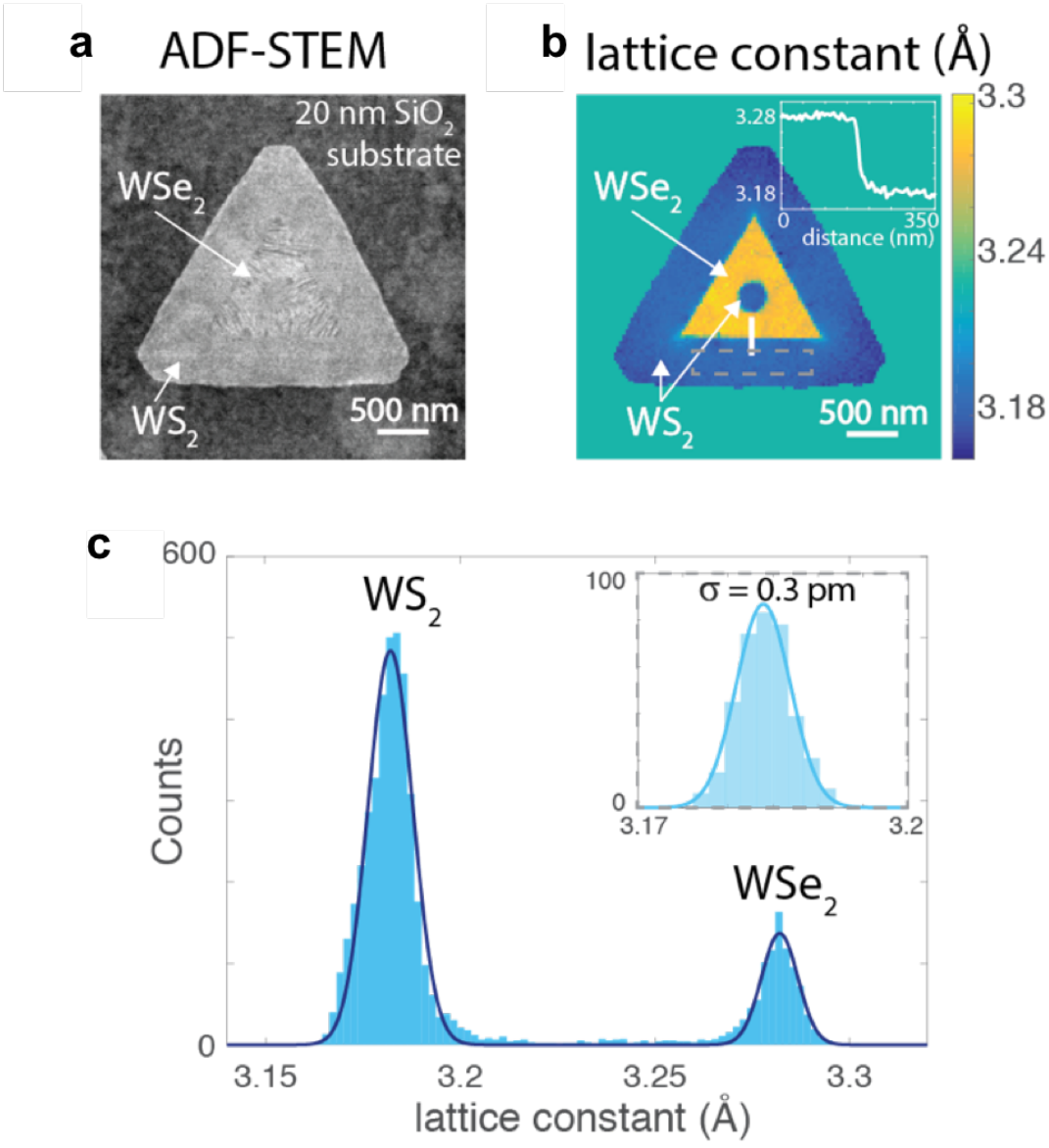

Figure 3.2: Lattice constant map by EMPAD. (a) ADF-STEM image extracted from the EMPAD 4-D data on a wide WS_2-WSe_2 lateral heterojunction. The inner detector angle is 50 mrad. (b) Lattice constant map of micron-sized triangles. The inset displays a line profile across the interface between WSe_2 and WS_2. (c) Lattice constant histogram from (b). The inset is the histogram from a flat region (gray box in (b)), indicating a precision of at least 0.3 pm.

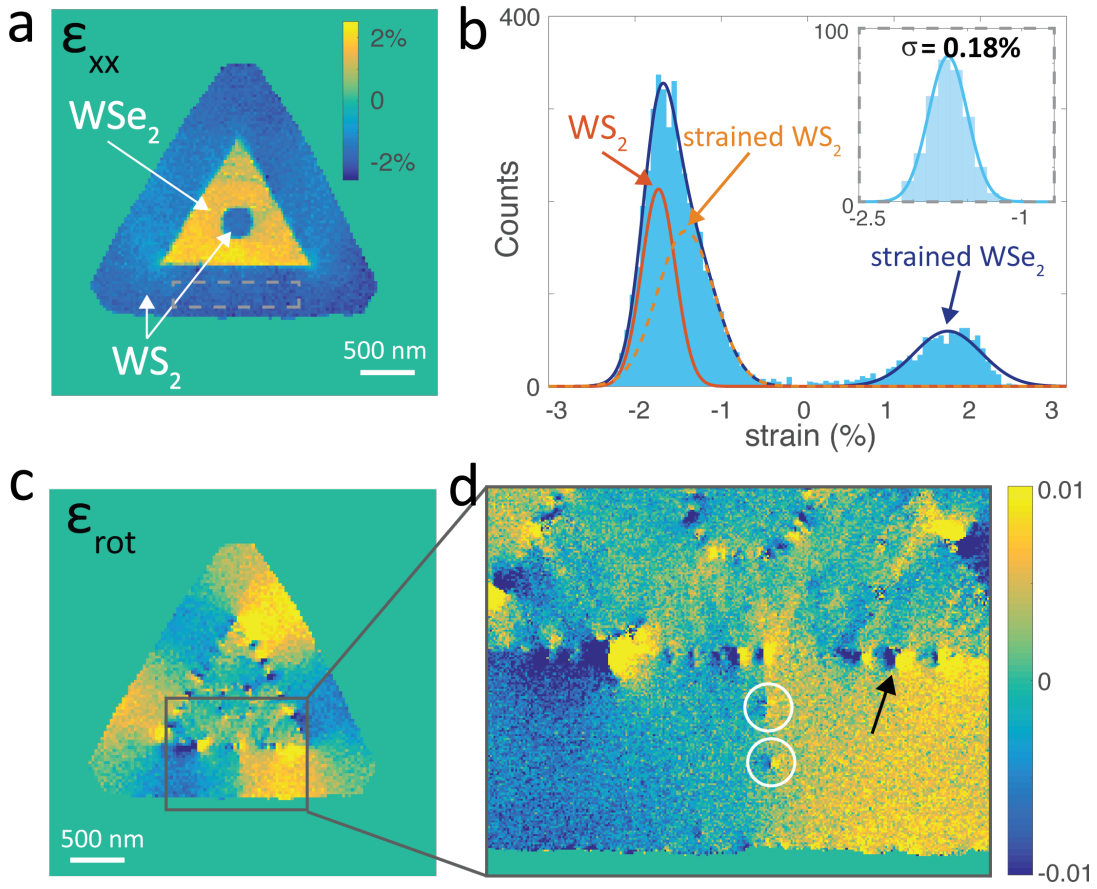

Figure 3.3: Strain maps by EMPAD. (a) Uniaxial strain map showing most of the strain has been released. (b) Strain histogram from (a) The WS_2 peak fits two Gaussians that correspond to unstrained and strained regions. The inset shows the histogram from a flat region (gray box in (a)) indicating a precision better than ~0.18%. (c,d) The rotation map displaying periodic misfit dislocations that contribute to relaxing the lattice strain at the WS_2-WSe_2 junction. The internal strain in WS_2 results in a few dislocations inside WS_2, which are indicated by the white circles.

approach to achieve a high angular resolution in the diffraction space for strain mapping. Appendix D.1 will describe the details of CoM measurements. More information of the lattice constant mapping can be found in Appendix D.2.

3.3.2 Strain and dislocations

From the CoMs of all diffraction spots, we extract the diffraction vectors g_i (i=1,2), i.e. the reciprocal lattice vectors, to map the strain and rotation across the heterostructure (see details in Appendix D.3). The x-direction uniaxial strain (ε_{xx}) map in Fig. 3.3 a shows clear differences between the WS_2 and WSe_2 as well as small local variations, indicating the film is largely relaxed, but not completely. This is expected since the width of the WS_2 is far beyond the *critical thickness*. To see the strain details, we plot the histograms of the x-direction strain map, where the WS_2 peak in Fig. 3.3 b fits two Gaussian peaks, corresponding to the unstrained (outer edges) and strained (interfaces) parts of the WS_2 lattice in Fig. 3.3 a. From a relatively flat WS_2 region (gray box in Fig. 3.3 a), we determined that the precision of our technique is at least 0.18%, as given by the spread of the histogram in the insert of Fig. 3.3 b.

The rotation map (Fig. 3.3 c) displays periodic misfit dislocations as dipole fields located at the interface between WS_2 and WSe_2. The misfit dislocations along the interface contribute to release the lattice strain. However, the observed misfit dislocation spacing (~100 nm) is much larger than the spacing required to fully relax the lattice strain caused by the 3.1% lattice mismatch between WS_2 and WSe_2 (~ 10 nm). We note an internal periodic strain field in the outer WS_2 region in the rotation map (Fig. 3.3 c). Analogous to bulk epitaxy, which forms periodic ripples within the top layers of the thin films [84], the periodic strain fields lower the elastic strain energy in 2-D heterojunctions and create additional dislocations inside WS_2, as depicted in the magnified rotation map (Fig. 3.3 d). However, the long wavelength of the strain field shown in the rotation map (Fig. 3.3 d) implies that it also plays a minor role in releasing strain.

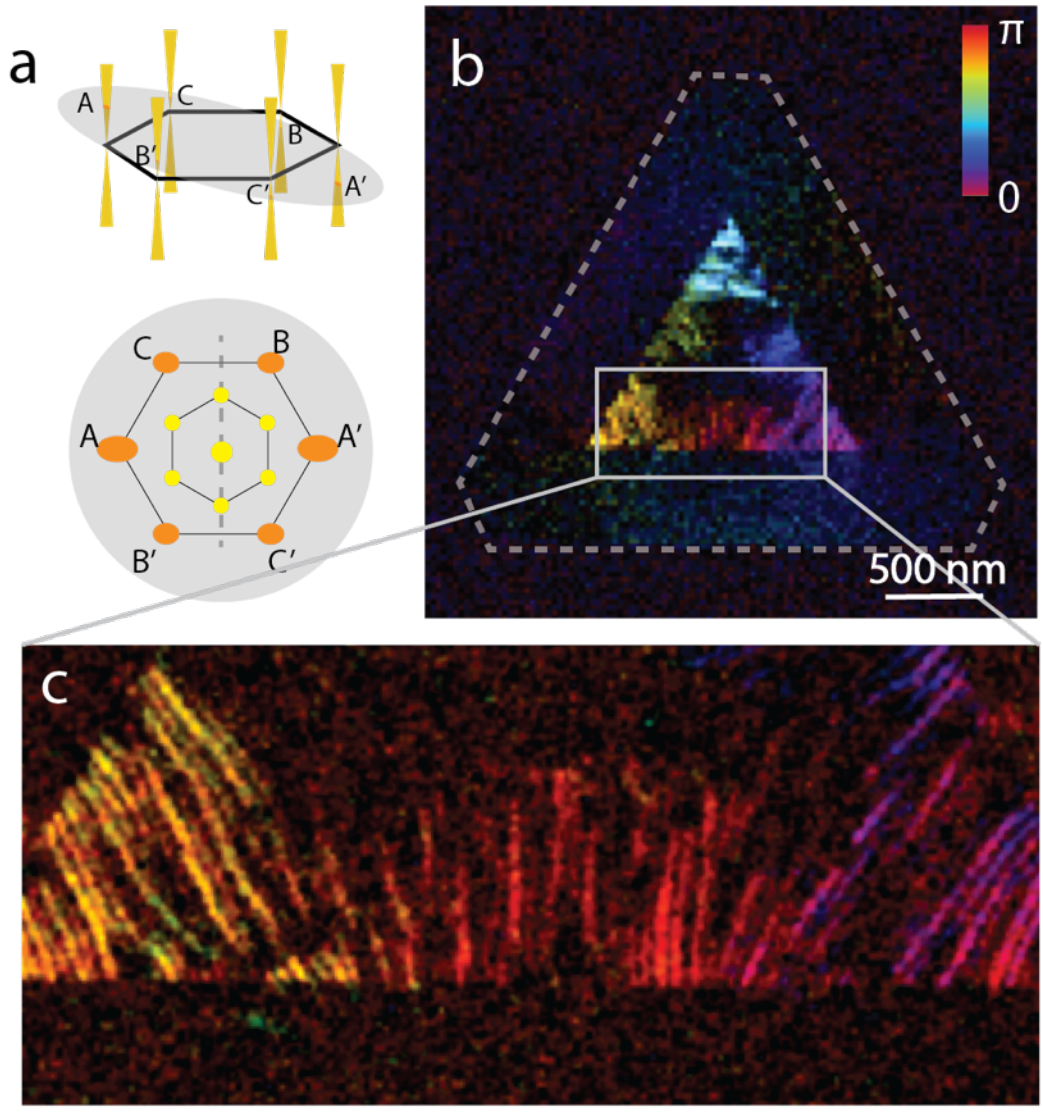

Figure 3.4: Map of out-of-plane ripples. (a) Schematics showing that a local sample tilt causes a broadening of the diffraction spots due to the intersection of the Ewald sphere with the cone-shaped diffraction rods resulting from thermal fluctuations in 2-D materials. The broadening of the measured diffraction spots was quantified from the second moment (i.e. mean squared width). (b) Map of the orientation of ripples calculated from the phase of the ripple measure, R. The map shows the WSe_2 film forms out-of-plane ripples to release the strain, while WS_2 is flat. (c) Magnified ripple map showing a nanoscale ripple array along the junction.

3.3.3 Periodic ripples

As stated before, both interfacial dislocations and the rotation strain fields cannot fully relax the lattice strain generated by the lattice mismatch. A more significant contribution for releasing strain is that 2-D materials can also buckle up and form out-of-plane ripples without introducing in-plane lattice distortions. We observed that the WSe_2 forms this type of ripples, which is the origin of WSe_2's broader peak in Fig. 3.3 b.

To accurately identify the out-of-plane ripples and quantitatively map their orientations, we developed a novel approach, using the EMPAD 4-D datasets. Thermal and static fluctuations in 2-D materials smear the diffraction rods into cones [85]. The diffraction pattern is formed where the Ewald sphere intersects the cone, and consequently the measured diffraction spot becomes broader as the macroscopic sample tilt is increased, as illustrated schematically in Fig. 3.4 a. For tilt angles up to about 30°, this is a linear relationship [85]. The diffraction spots have a roughly Gaussian intensity profile, so we measure their widths from their second moments – i.e. the mean square angular width. Here, we mapped the tilted regions (i.e. the macroscopic ripples) by measuring the relative broadening of the diffraction spots compared to flat regions. We defined the complex ripple measure as $R = A + Be^{i2\pi/3} + Ce^{i4\pi/3}$, where A, B, and C are the characteristic widths (as measured by second moments) of the corresponding diffraction spots in Fig. 3.4 a. The amplitude of R captures the magnitude of the local tilt in the ripple, while the phase gives the orientation of the ripples. As illustrated in the phase plot of the R maps (Fig. 3.4 b), the ripples form along different orientations, and only appear inside WSe_2. In addition, the ripples prefer to form perpendicular to the interface between WS_2 and WSe_2 on the WSe_2

side, thus releasing the lattice strain, as shown in Fig. 3.4 c. (More details can be found in Appendix D.4)

3.4 Narrow WS_2–WSe_2 heterostructures

These aforementioned methods can also be applied to narrow multi-junction lateral heterostructures [49], where the width of each WS_2 or WSe_2 is only ~ 100 nm. The strain maps (Fig. 3.5 a and b) present a strong uniaxial strain in the sample along the directions parallel to the hetero-interfaces, leading to a coherent superlattices of 2-D lateral heterojunctions with a periodicity of ~ 200 nm. In addition, the rotation map (Fig. 3.5 c) contains a few dipoles that are the misfit dislocations. Considering the flake size and number of the multijunctions, the influence of these topological dislocations on the overall lattice structure, as well as its optical and electrical properties, becomes ignorable. As a result, we can conclude that the superlattice is almost free of dislocations, confirming the strain accomodation and lattice coherency in the superlattices. Fig. 3.5 c also reveals the minor internal strain in narrow lateral heterostructures. Compared to broad junctions (Fig. 3.3 c), the periodic rotation strain fields in narrow ones are much weaker, and thus avoid the internal dislocations caused by these strain fields. In addition, the strain fields form domains with much sharper boundaries than those in the broad lateral heterostrucures, which may caused by the high spacial frequency of the narrow junction superlattices. Although each layer in the superlattice contains strong uniaxial strain, WSe_2 still forms periodic ripples as shown in Fig. 3.5 d. These ripples have an aspect ratio of ~ 1:50 (height to width) on average according to atomic force microscopy (AFM) [49], indicating a minor influence on releasing the lattice strain.

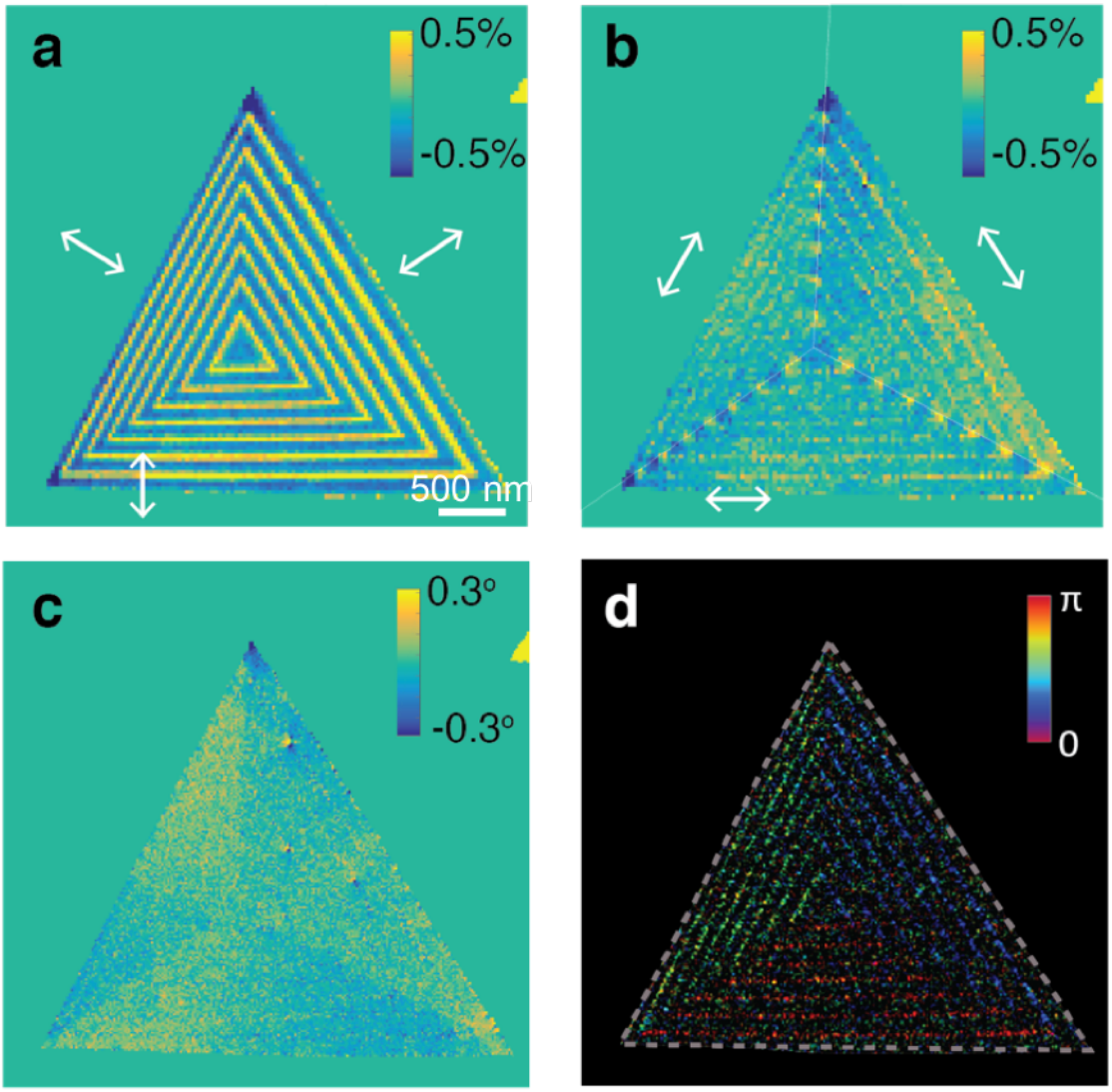

Figure 3.5: EMPAD maps of narrow heterostructures. (a) Uniaxial strain map showing the strain along the directions perpendicular to the multi-junction interfaces. (b) Uniaxial strain map displaying the strain along the directions parallel to the multi-junctions. (c) Rotation map that picks up three misfit dislocations in the triangle flake. Compared to the flake size (in microns), these three misfits are negligble. The internal strain causes the small periodic rotation fields across the flake. (d) Ripple map that shows ripples in WSe_2.

3.5 Conclusion

In conclusion, we developed an approach to map lattice constant, strain, dislocations, and out-of-plane ripples with high precision on all relevant length scales. All lattice information can be extracted from the 4-D data which requires only a single fast scan, effectively reducing the electron dose in 2-D materials. Moreover, the accuracy of CoM measurements allows us to map the lattice constant and strain with precisions greater than 0.3 pm and 0.18 % respectively in 2-D materials. The approach to map out-of-plane ripples can uncover small tilts ranging from less than 1° to 30°. In addition, our approach may also be valuable for studying other lattice distortions in 2D materials, and thus provide essential feedback for material synthesis.

By using the EMPAD, broad and narrow lateral heterojunctions were examined. In broad lateral heterojunctions, we observed that the lattice strain is mostly released by misfit dislocations and out-of-plane ripples. In contrast, the narrow lateral heterojunctions form coherent superlattices with strong uniaxial strain, while containing minor misfits and ripples that partially release small amount of the strain. These achievements uncover the fundamental strain relaxation mechanism in epitaxial 2-D lateral heterojunctions, where the misfit dislocations and internal rotation strain fields perform similarly as those in their bulk counterparts, while the ripples presented here are novel and unique in 2-D materials.

CHAPTER 4

GRAPHENE–MOS_2 LATERAL HETEROSTRUCTURES

This chapter was adjusted from our paper: Mervin Zhao, Yu Ye*, Yimo Han*, Yang Xia*, et al. "Large-scale chemical assembly of atomically thin transistors and circuits" Nature Nanotechnology 11, 954-959 (2016). Our electron microscopy data have uncovered very important structural information that gives insight into the growth mechanism and elucidates the high performance of the device.*

4.1 Introduction

Single-layer graphene has excellent conductivity, making it ideal for the interconnections and wiring of next-generation devices [6, 18, 20]. To fabricate devices out of 2-D materials, the spatially controlled synthesis of conductor-semiconductor heterostructures is a necessary step towards achieving full atomically thin circuitry. However, graphene and semiconducting TMDs possess dissimilar lattice structures, making them trivial to merge seamlessly in the lateral dimension. This chapter will describe how they laterally join together, which not only determine the mechanical strength and device performance, but also can give insight into the growth mechanism.

4.2 Sample growth and fabrication

To chemically assemble the heterostructures, single-layer graphene was first transferred onto a silica substrate (large-scale growth and transfer techniques

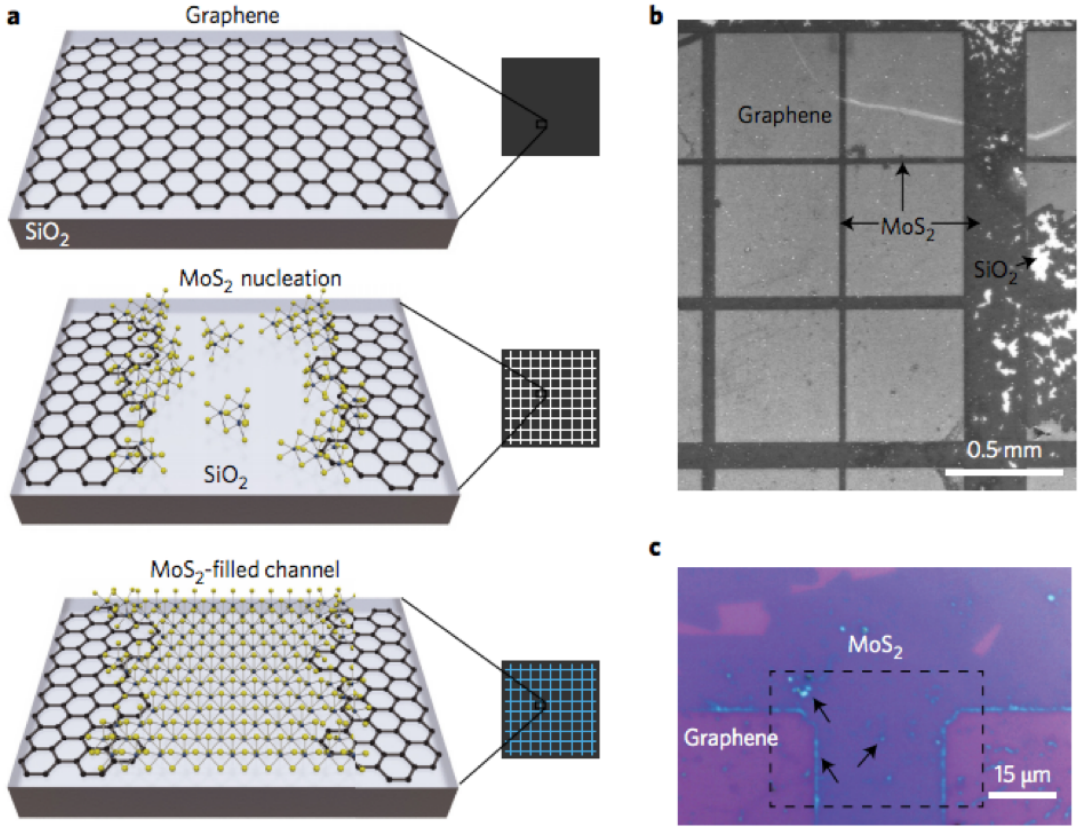

Figure 4.1: Growth schematic and large-scale characterization of the graphene-MoS_2 heterostructures. (a) Scheme of the heterostructure growth process. Graphene is first etched into channels and MoS_2 begins to nucleate around the edges and within the channel. On the edges, MoS_2 forms a thicker overlap junction with the graphene. Finally, further growth results in MoS_2 completely filling the channels. (b) Scanning electron microscope image of the chemically grown MoS_2 between the edges of the graphene. The image shows a large scale of coverage, on a millimeter scale. (c) Optical image of the heterostructure. Within the narrow channel, the MoS_2 fills the area between the graphene sections. Thicker areas are observed around the edges of the graphene, indicative of nucleation of the MoS_2 areas (marked by the black arrows).

for graphene are now common [18,20]). Patterns of channels were defined using oxygen plasma. The patterned graphene on a silicon wafer was then placed into a quartz tube for seed-promoted CVD growth of single-layer MoS_2 [21]. Preferential growth within the SiO_2 channels results in the merging of individual domains, which form a continuous, polycrystalline single layer of MoS_2, consistent with the observations made with large-area chemical vapor growth on bare substrates [19,21,22]. More details of the growth can be found in reference [42].

To transfer the sample on to a TEM grid, the polymer transfer approach was utilized. The sample was first coated with polypropylene carbonate (PPC), a polymer lighter than PMMA. Afterwards, the substrate was etched with potassium hydroxide (KOH) solution to release the film (including PPC and 2-D materials). After rinsing in DI water, the film was transferred to holey carbon grids. The polymer was removed by vacuum baking. Details for transferring samples from Si/SiO_2 substrates can be found in Appendix B.2.

4.3 Interface structures

To uncover the atomic structures at the lateral heterojunction interfaces, several conventional TEM techniques were employed. The dark field TEM [26,28] provided the complete grain orientations of MoS_2 and graphene. ADF-STEM as the primary choice for high-resolution characterization offered both atomic structures and thickness maps of the graphene-MoS_2 lateral heterojuncitons. Since the intensity of ADF-STEM scales with the atomic number square, the junction interfaces and number of layers of both graphene and MoS_2 can be clearly visualized. Finally, EELS provided the compositional information, as

well as the bonding from the fine shape of the peaks in the spectrum. The EEL spectrum confirmed that there is no bonding between the two crystals, indicating a vdW coupling between MoS_2 and graphene.

4.3.1 Grains and grain orientations

The poly-crystallinity nature (the grain size and grain orientations) of chemically synthesized 2-D materials affect their properties. We evaluated the crystallinity of the grown single-layer MoS_2 as well as the junction between the MoS_2 and graphene using dark field TEM. Fig. 4.2 a shows a bright field TEM image of the lateral heterojunction interface that was suspended over a hole in the TEM grid. The dark field TEM images of graphene and MoS_2 are used to create a false-color map of the heterostructure (Fig. 4.2 b) with diffraction pattern shown in Fig. 4.2 c. Mapping red to MoS_2 and yellow to graphene, an orange colored line is observed in the overlapped region, indicating a finite overlap of the two crystalline layers. The roughness of graphene edges are generated by the plasma etching during the patterning process. Both graphene and MoS_2 have a single grain orientation within the field of view of Fig. 4.2 b.

The larger scale false-color map (Fig. 4.2 d) shows the MoS_2 grain size can range a few micrometers near the graphene edge, with grain orientations independent of the graphene lattice orientation (Fig. 4.2 e). In addition, the MoS_2 at the lateral heterojunction interface contain bi- or multi-layers, suggesting a high nucleation density along the graphene edges during the growth.

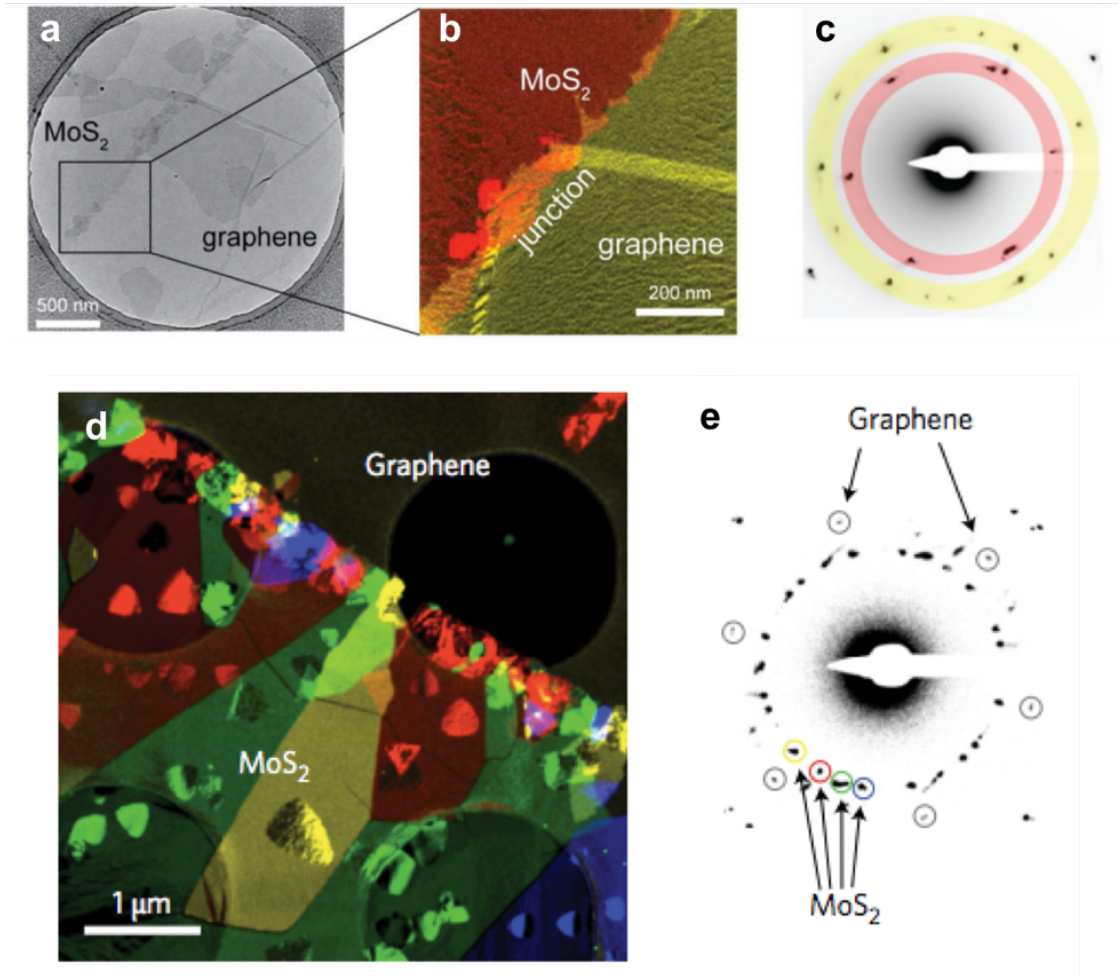

Figure 4.2: Dark field TEM of the graphene-MoS_2 lateral heterostructures. (a) Bright field TEM image of suspended MoS_2-graphene junction. (b) False-color dark field TEM overlay of the MoS_2-graphene junction. The graphene region is mapped to a yellow color, while the MoS_2 region is mapped to a red color. The overlap junction, shown as an orange color, is a finite overlap between of the two layers. (c) Diffraction pattern of the image shown in (b) with two rings corresponding to the MoS_2 and graphene diffraction spots. The grains corresponding to these areas are mapped to the false-color map. (d) False-color dark field TEM overlay showing the MoS_2 is continuous and polycrystalline at the graphene-MoS_2 junction. The MoS_2 grains show random orientations with respect to the graphene. (e) Corresponding diffraction pattern from the region in (d) indicates the graphene is single crystal. The four colored circles indicate distinct grain orientations of the MoS_2 used to create the false-color map in (d).

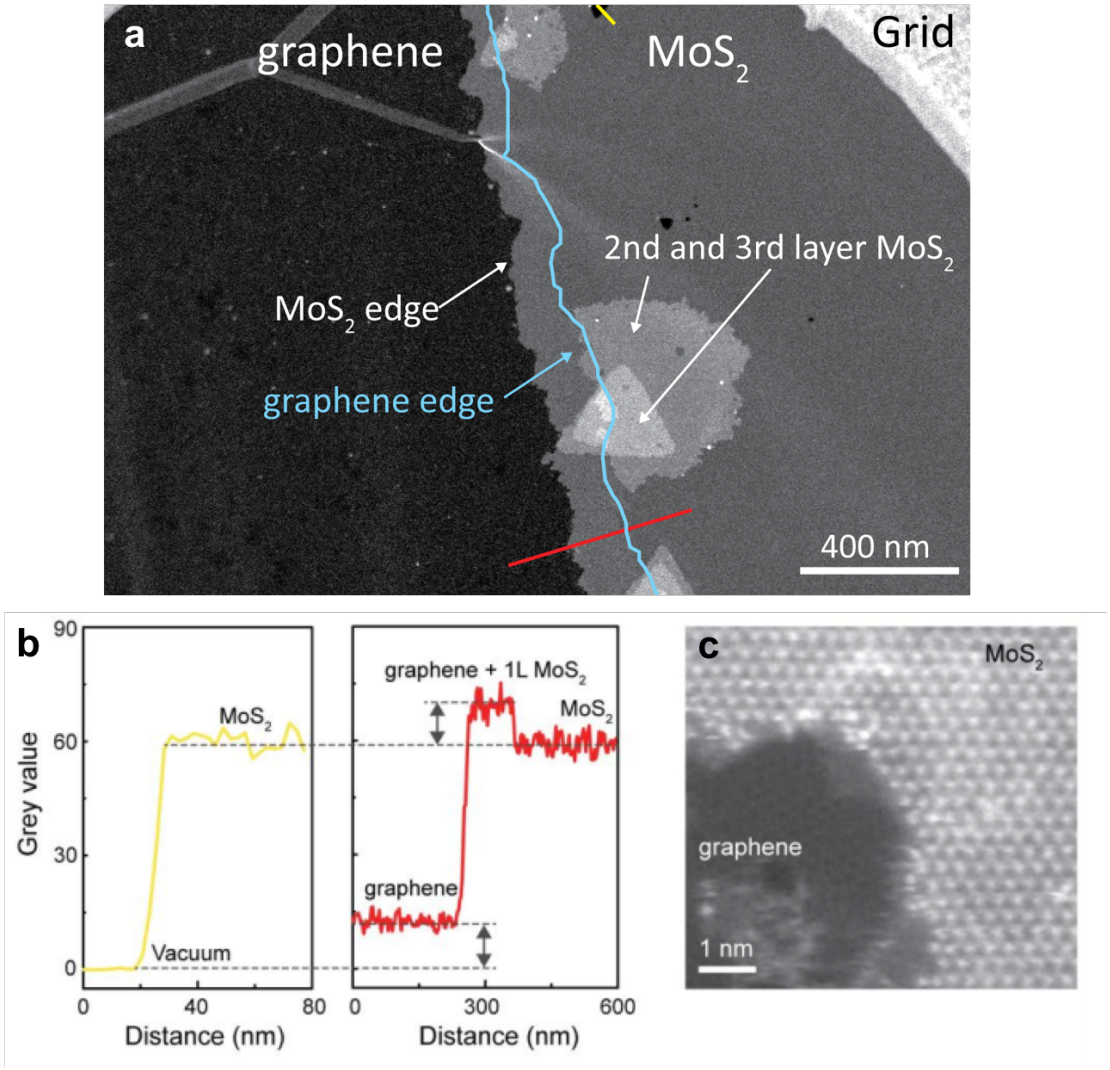

Figure 4.3: ADF-STEM images of the graphene-MoS_2 lateral heterojunctions. (a) The large scale ADF-STEM image showing an overlap of ~ 100-200 nm. The graphene edge was identified by the image intensity. (b) Corresponding intensity line profile from the red (yellow) line across the junction (a hole) in (a). From the line profiles, we can distinguish the vacuum, graphene, MoS_2, and the overlapped junction region from their ADF image intensity. (c) Atomic resolution ADF-STEM image of the junction, showing the crystalline nature of MoS_2 in the junction. The graphene atomic structure is not as clear due to the scaling of the intensity ($\sim Z^2$).

4.3.2 Atomic structures

In order to answer how graphene and MoS_2 merge atomically, ADF-STEM was used to provide high-resolution images of the graphene-MoS_2 lateral heterojunction (Fig. 4.3 a). Using intensity plots from line profiles in the image (Fig. 4.3 b), it was possible to elucidate that the junction is a ~ 100nm overlap of single-layer MoS_2 on top of graphene. In addition, further growths of secondary and tertiary patches of MoS_2 were observed close to the graphene edge, though never growing within the graphene surface. This confirms that nucleation of the MoS_2 occurs at the edges of graphene, with defects of the graphene-MoS_2 junction allowing multilayer patches to grow. In addition, both graphene and MoS_2 retain their crystalline nature, as observed in an atomic-resolution ADF-STEM image of the junction in Fig. 4.3 c. Due to the large atomic number difference between carbon and molybdenum atoms, the graphene side shows only hints of lattice, while the overlapped region dominates by MoS_2 lattice.

4.3.3 Elemental information

The nature of the overlapped junction between graphene and MoS_2 can also be probed using EELS, which provides compositional and bonding information for the heterostructure. From the spectrum in Fig. 4.4 a, the carbon K-edge is used to identify graphene, while distinct molybdenum and sulfur edges can be used to identify the MoS_2. Using the distinct graphene signature (σ^*) and the sulfur edges for MoS_2, a compositional map can be created (Fig. 4.4 b). Within the overlapped region, the lack of additional new peaks as well as the retention of graphene and MoS_2 signatures confirms that the overlap is a vdW hetero-

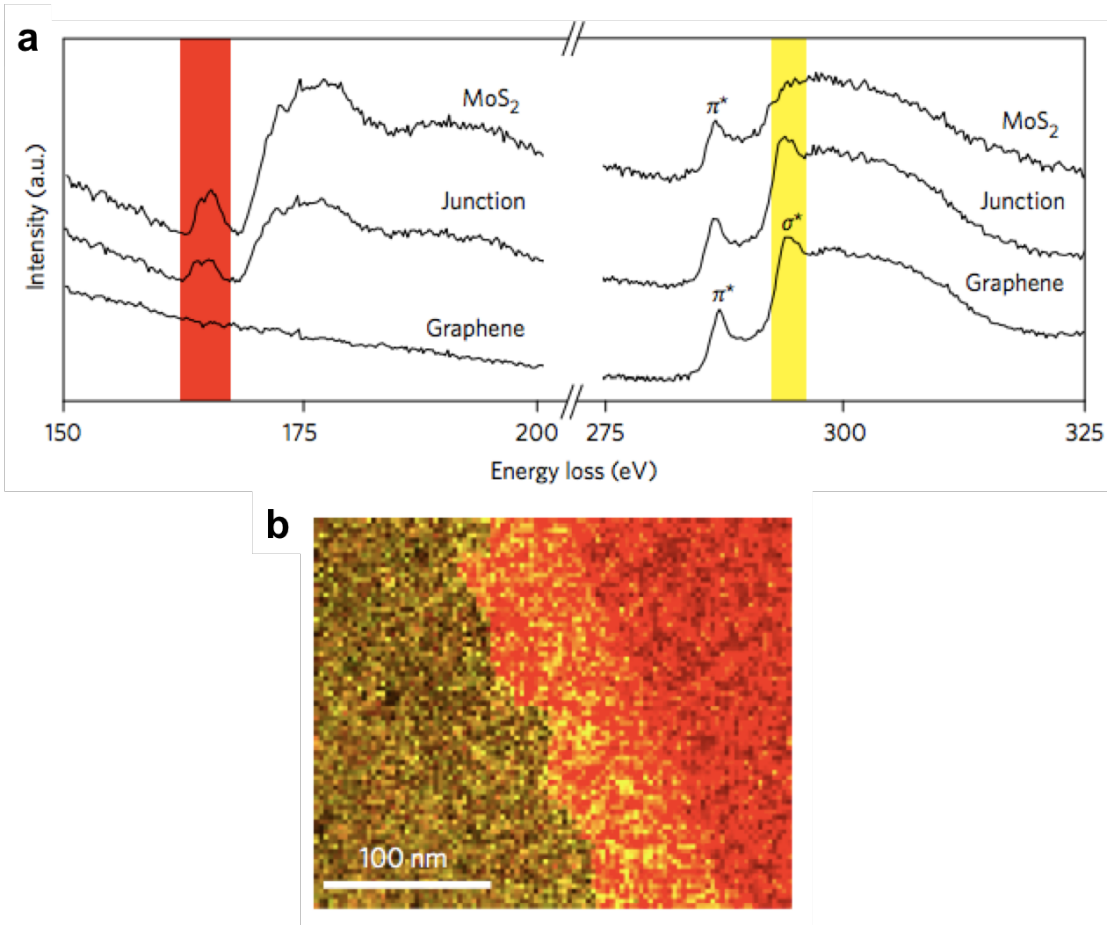

Figure 4.4: EELS of the graphene-MoS_2 lateral heterojunctions. (a) EELS spectra of graphene, MoS_2 and the junction show S and C edges. The graphene signature in the σ^* peak shows up on the graphene and the junction, while only amorphous carbon (π^*) from the polymer residue shows up on the MoS_2. (b) Elemental EELS map of graphene (yellow) and MoS_2 (red), confirming the overlapped junction. The graphene and MoS_2 maps are integrated from the yellow and red regions, respectively, of the spectra in (a) using multiple linear least-squares (MLLS) fitting.

junction without the formation of additional covalent bonding in the energies probed. This vdW heterojunction gives rise to an atomically thin Ohmic contact suggesting efficient charge flow between graphene and MoS_2.

4.4 Conclusion

As a summary, TEM study uncovers the nanometer-scale overlapped graphene-MoS_2 lateral heterointerfaces. The dark field TEM images indicate an independent poly-crystallinity nature between graphene and MoS_2, while the ADF-STEM images present more details of the film thickness, revealing the overlapped junction region and multilayer MoS_2 regions. EELS confirms the overlapped junction and validates the vdW interaction between graphene and MoS_2 at the junction.

These results indicate a reduction in the nucleation energy barrier of MoS_2 at the edges of graphene compared with its surface. Growth on the graphene is limited due to difficulties with the vertical epitaxy of MoS_2 on graphene, as large crystalline areas require unique growth conditions that are not present in this particular growth [86]. Thus, we summarize the growth process as edge nucleation and the formation of an overlap junction encouraged by defects in the graphene, combined with MoS_2 filling through seeded growth on hydrophilic areas. Different from lateral epitaxy of dissimilar TMDs, the lattice mismatch (in- and out-of-plane) as well as distinct chemical differences between graphene and MoS_2 inhibit in-plane bonding and epitaxy, leading to the formation of an overlap junction.

CHAPTER 5

CONCLUSIONS

5.1 Summary

Since two-dimensional materials are a promising class of materials for future electronics, their lateral heterostructures were intensively fabricated and studied. This dissertation uses TEM to address the atomic structures of 2-D lateral heterojunctions. In particular, STEM with the ADF detector and the EMPAD provides high precision structural information that are crucial for understanding properties that may be relevant to future electronic applications.

Three projects are discussed in this dissertation:

- Chapter 2 has demonstrated atomically sharp lateral heterojunctions of MoS_2 and WSe_2. Atomic resolution ADF-STEM combined with GPA method has been employed to uncover the strain and misfit dislocations at the abrupt interfaces. The results show that at a broad junction (micrometer scale), periodic misfit dislocations decorate the atomically sharp interface and contribute to a strain relaxation in MoS_2 and WSe_2. In contrast, at narrow junctions (sub- to two-nanometer scale), coherent interfaces that are free of dislocations are observed. These narrow channels can be grown from a dislocation catalyzed approach [48], where dislocations climb and leave the embedded channels behind them.
- Chapter 3 has introduced WS_2-WSe_2 lateral heterostructures. In order to elucidate the lattice structures at the interface, a novel approach exploiting the EMPAD has been developed to map the strain of 2-D materials with

sub-picometer precision. At broad junctions (~500 nm), periodic misfit dislocations and ripples are the main contributions to relax the strain caused by the lattice mismatch between WS_2 and WSe_2. In comparison, narrow junctions (~100 nm) possess strong uniaxial strain and maintain the lattice coherency. Some dislocations and small out-of-plane ripples are also observed in narrow junctions, but their influence is negligible.

- Chapter 4 discussed graphene-MoS_2 lateral heterojunctions. Combining the conventional dark field TEM, ADF-STEM, and EELS, the overlapped lateral hetero-interfaces between graphene and MoS_2 with a vdW interaction are confirmed. The results provide insights into the growth mechanism of the graphene-MoS_2 lateral heterostructure, indicating a preferential overlap junction forms between two different 2-D materials with distinct chemical differences and dissimilar lattice structures.

5.2 Future directions

As an extension of our work, there are many potential future directions which can arise from the results presented in this dissertation. First of all, the lateral heterostructure platform contains a number of combinations that provide all necessary components for atomically thin circuitry. Since more and more 2-D materials are being discovered, the possible combinations of 2-D crystals for lateral heterojunctions are expanding. According to the knowledge that has been gained from this dissertation, below are my personal suggestions for future studies, including optimal material choices, structural preferences, and synthesis challenges.

- 2-D materials to fabricate lateral heterojunctions should adopt a similar lattice structure, thus allowing for seamless epitaxial interface forming between the two materials. As an example, TMDs are a group of 2-D materials possessing a similar sandwiched lattice structure. We have demonstrated the lateral heterojunctions between two semiconductors (Chapter 2 and 3). Within the TMD group, some metallic 2-D films such as tungsten ditelluride can be predicted to be excellent metallic interconnects for semiconducting TMDs. A wise choice of the material combinations should be considered in advance.
- Narrow lateral heterojunctions are always preferred. There are two reasons for this: As discussed in Chapter 2 and 3, narrow junctions effectively avoid misfit dislocations at the lateral hetero-interfaces, providing strain accommodation and lattice coherency. In addition, because narrow junctions shrink the lateral dimension comparing to broad ones, they benefit the ultimate scaling of the electronic devices.
- Large-scale chemical assembly with high spacial precision and clean junctions remains challenging. Currently, the geometry of the epitaxial lateral heterojunctions is set by the shape of the originally grown flake, since the following materials are all grown epitaxially from the edge. For example, the epitaxial lateral heterojunctions that have been described in this dissertation are all in triangle shape. Wafer-scale chemical assembly with precise and controllable junction locations are crucial for the potential electronic applications of 2-D materials

Secondly, new techniques to uncover structures in 2-D materials are also highly relevant. Rather than lateral heterojunctions, 2-D materials can also be

used to create more complex structures such as kirigami [87], origami [88], and corrugated films. To uncover their atomic structures, conventional TEM techniques are not sufficient anymore. We need to keep this in mind and push new electron microscopy techniques, new data processing approaches, and even new TEM sample fabrication methods. All these aspects are worth exploring.

Last but not least, our EMPAD can be combined with other state-of-the-art techniques such as cryo-EM to study challenging materials beyond 2-D lateral heterojunctions, such as metal organic frameworks and even biological molecules. These materials are extremely sensitive to damage from the electron beam, so that the high speed and high sensitivity of the EMPAD will offer dramatic advantages to study these dose-limited materials in STEM mode.

APPENDIX A

TIPS FOR CROSS-SECTIONAL SAMPLE PREPARATION

Cross-sectional TEM is essential to study van der Waals heterostructures. Typical focused ion beams (FIB) systems have the capability to make cross sections out of materials. General lift-out procedures have been developed and can be found in reference [89]. However, the uniqueness of 2-D materials requires new strategies to fabricate FIB lamellas. Below is a summary outlining tricks for cutting 2-D materials on substrates.

A.1 2-D flakes aligned with the substrate

Typically, in order to examine a cross-sectional sample in electron microscope with atomic resolution, the sample has to be tilted to the correct orientation where columns of atoms are aligned with the electron beam, so that the projection of each atomic column appears to be a dot in the image. However, this is a major limitation for 2-D samples. The crystal orientations of 2-D materials are randomly distributed and misaligned with the crystalline substrate that has to be used as the indication of the zone axis in microscopes. As a result, most 2-D materials cannot provide atomic resolution images from their cross-sectional lamella, such as the one shown in Fig. 1.4 a, where a multi-stack of continuous CVD TMDs has been examined.

To overcome this limitation, one strategy is to grow TMDs in a triangular shape and manually select the hero flake that aligns with the substrate. Since the substrates are usually diced along the crystal orientation, TMDs that are aligned with the substrate can be identified by their relative orientations (as shown in

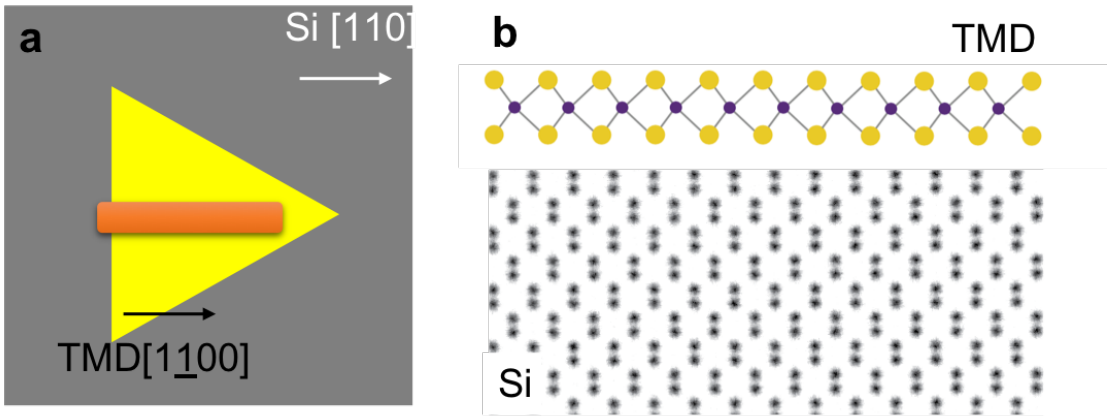

Figure A.1: Sample-substrate alignment. (a) Schematic of the sample-substrate alignment in FIB. The yellow triangle represents for the TMD sample. The gray box is the silicon substrate. Their crystal orientations are indicated by black and white arrows. The orange bar indicates the protecting Pt bar deposited in FIB. (b) A schematic of the lattice of cross sectional image when the alignment in (a) is employed.

Fig. A.1 a). The TMD orientation is good enough if the misalignment between the TMD flake and the substrate edge is within one degree. The orange bar in Fig. A.1 a is where the Pt protecting layer should be deposited to protect the specimen below it. Using this geometry to cut the FIB lamella, the final crystal orientations of both TMD and silicon substrate is shown in Fig. A.1 b. Thus, by tilting the cross-sectional lamella to the zone axis of the silicon substrate, TMD will also be on its zone axis, where atomic resolution images of the TMD cross-section can be acquired.

Beyond the scope of this study, this trick can also be extended to other types of 2-D specimens, such as exfoliated flakes which are quite common not to follow the substrate crystal orientation. In these samples, it is crucial to identify the crystal orientation of the target flake via its long straight edges and transfer the flake to a substrate in the aligned orientation. This requires dry transfer techniques which have been widely used for exfoliated samples [90,91].

A.2 Deposit protecting layers

Layers to protect the 2-D materials are extremely important to prevent ion beam damage. The atomically thin monolayers are on the very top of the sample. Thus, any exposure to the ion beam will destroy them. Two approaches were used to deposit the protecting layers for 2-D materials:

- For continuous films where no specific regions are targeted, a sharpie pen was used to draw small dots on the samples. A soft-tip sharpie is preferred since hard ones can scratch and tear the 2-D films. After an over-night dry, the sharpie marks became thin layers of amorphous carbon. Once a flat region was spotted on the sharpie mark, the Pt protecting bar was deposited directly on top of it using the ion beam at 30 kV. Then the general lift-out procedure was followed to finish the cutting. The sharpie layers are usually 0.5-1 µm thick, which is an ideal thickness to protect the 2-D films from ion beam damage.
- For a specific triangle (or an exfoliated flake), the electron beam in FIB was employed to deposit the Pd bar. These samples, if covered by the sharpie mark, would become invisible in FIB. Instead, a thin layer of carbon (~10 nm) was sputtered onto the entire sample, allowing for the target flake remaining visible. Afterwards, a ~ 20 nm-thick Pt bar was deposited at the target location by electron beams, which is slower than ion beams but safe for 2-D materials. Thereafter, with this Pt protection, it was safe to switch to ion beam and deposit more Pt up to ~1 µm before the general cutting and lift-out procedure.

APPENDIX B

IN-PLANE SAMPLE PREPARATION METHODS

2-D materials grow on a variety of substrates. To study their in-plane structures in TEM, releasing them from their original substrates and transferring them to TEM grids are necessary. Below, is a summary of the methods that I used to transfer TMDs on sapphire (adapted from Lain-Jong Li's group) and SiO_2 (adapted from Jiwoong Park's group) to TEM grids.

B.1 2-D materials on sapphire substrates

Sapphire is a common substrate to grow TMDs [19, 39]. It generates a very strong vdW force that keeps the TMD films flat. Although sapphire is transparent to light and enables easy access to many optical transmission measurements, it is not transparent to electron beams due to its thickness and high density. In order to use TEM to study the lattice structure of TMDs, TMDs have to come off from the sapphire substrate and to be placed on TEM grids that contain holes or very thin supporting layers (usually 5-20 nm). The following steps summarize the transfer procedure (schematics in Fig. B.1):

1. The sample (TMDs on the sapphire) was coated with PMMA 950K A4. A speed of 1000 rpm was used to spin coat for one minute. Then the sample was baked at 90 °C for 30 seconds to dry and fix the PMMA.
2. The specimen was soaked in hydrogen fluoride solution (HF:H_2O = 1:3 in volume) for 15~20 min, allowing the HF to etch the sapphire beneath the TMDs.

3. Before the film (TMDs and PMMA) was detached from the substrate, the sample was taken out of the HF solution and was soaked in de-ionized (DI) water to bath more than five times (5 minutes each) to dilute and clean the HF.
4. The film was gently peeled off using a sharp tweezer, assisted by the surface tension of the DI water.
5. A TEM grid was used to fish up the suspended film that floats on the DI water. The TEM grid was then air dried.
6. The grid was baked in ultra-high vacuum (10^{-7} Torr) at 350 °C for 5 hours to remove the PMMA.

The most challenging step was to peel off the film from the substrate (step 4). To tackle this challenge, my suggestion is to start peeling from the edges, similar to peeling tape from a surface. If you observe that the sharp tweezer tears the film, it means the PMMA layer is probably too thin. The thickness of the PMMA can be increased by either reducing the spin-coating speed or increasing the number of PMMA layers. However, thick PMMA sheets are hard to bake off entirely, and it may lead to dirty TMDs in TEM. The ideal thickness is about four hundred nanometers.

B.2 2-D materials on SiO_2 substrates

TMDs also grow on silica [22], which is a relatively typical material covering the surface of silicon wafers. One advantage of using silicon wafers to grow TMDs is that TMDs can be directly fabricated into electronic devices to measure

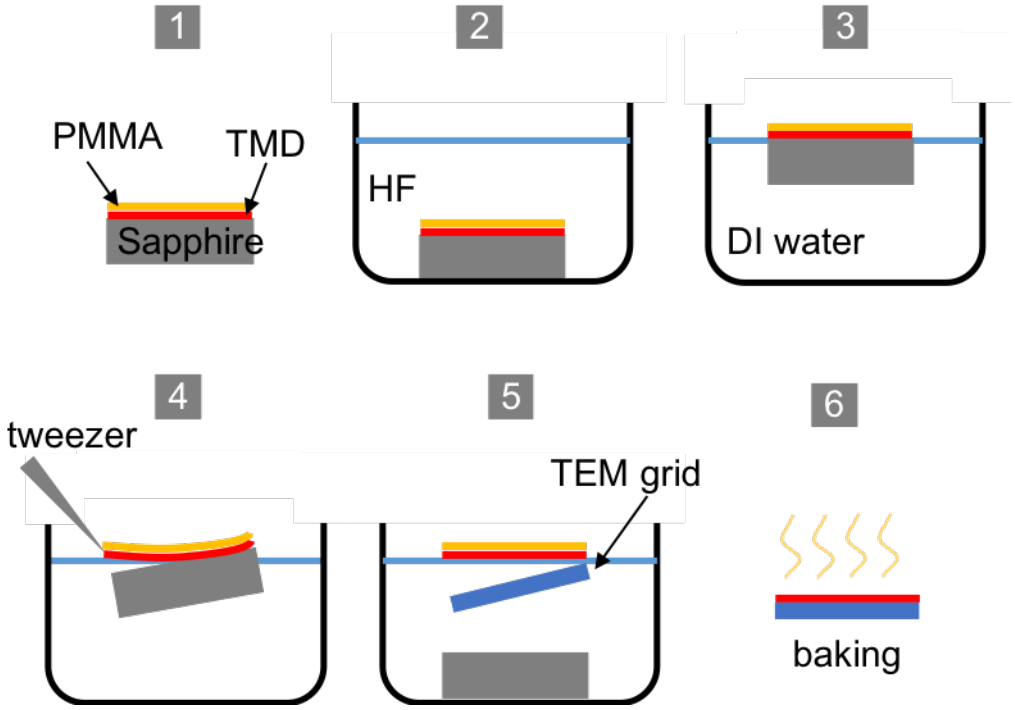

Figure B.1: Schematics of transferring TMDs from sapphire substrates to TEM grids. The numbers in this figure follows the procedure demonstrated in the text.

electrical properties. In addition, the vdW interaction between TMDs and silica is much weaker in comparison to using sapphire substrates. Therefore, the TMD films can be picked up by tapes and other 2-D materials or they can be easily released by water delamination using surface tension. The water delamination provides a straightforward approach to transfer continuous TMDs to TEM grids: just to delaminate and pick up. Although the delamination approach by DI water does not involve polymers during the transfer process, TMDs still absorb hydrocarbon residues from the DI water. Bake-out after the transfer is always preferred.

In contrast, discontinuous TMD flakes are very difficult to be scooped up after water delamination. Polymer supports are required for the transfer process. Below I describe the transfer process for 2-D materials on silica substrates:

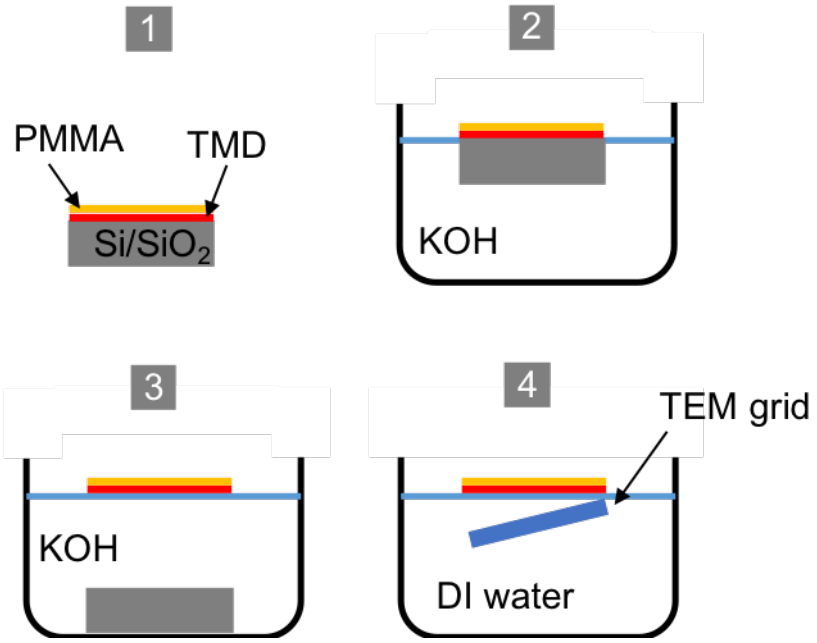

Figure B.2: Schematics of transferring TMDs from Si/SiO_2 substrates to TEM grids. The numbers in this figure follows the procedure demonstrated in the text.

1. The sample (TMDs on the silicon chip) was spin-coated with PMMA 495K A4 at a speed of 3000 rpm for one minute. Then the sample was baked at 90 °C for 30 seconds to dry and fix the PMMA.
2. The chip was gently placed on a KOH solution (1 Mol/L), where the chip floated on the solution.
3. After the film (TMDs and PMMA) detached from the silicon substrate which sank to the bottom, the film was scooped from the KOH solution and transferred to DI water to clean off the KOH residues.
4. The film was fished using a TEM grid and baked in ultra-high vacuum (10^{-7} Torr) at 350 °C for 5 hours to remove the PMMA.

APPENDIX C

GPA STRAIN MAPS

C.1 Requirements for the ADF-STEM images

Geometric phase analysis (GPA) is a method for measuring and mapping strain fields from high-resolution electron microscope images [77]. It describes how the spatial frequency components (lattice fringes) of the image vary across the image field of view. Therefore, it requires atomic resolution images without scan distortion. As we know, ADF-STEM scan noise can be effectively removed by averaging multiple cross-correlated images. I always use stacks of images (10~20) and the scan noise averages out.

C.2 Mapping strain

We used the GPA plugin developed for Digital Micrograph, and the detailed process was described below and in Fig. C.1.

1. Fourier transform the lattice image: We firstly Fourier transform the atomic resolution images (Fig. C.1 a) to the power spectrum (Fig. C.1 b). In the power spectrum, the strong Bragg-reflections are related to the unit cell of the crystalline structure of the material. A perfect crystal lattice gives rise to sharply peaked frequency components, while the broadening of the Bragg spots is due to the local lattice distortion in the material.
2. Place masks: Instead of using a mask covering the entire first Brillouin zone, practically we placed circular Gaussian masks on two non-colinear

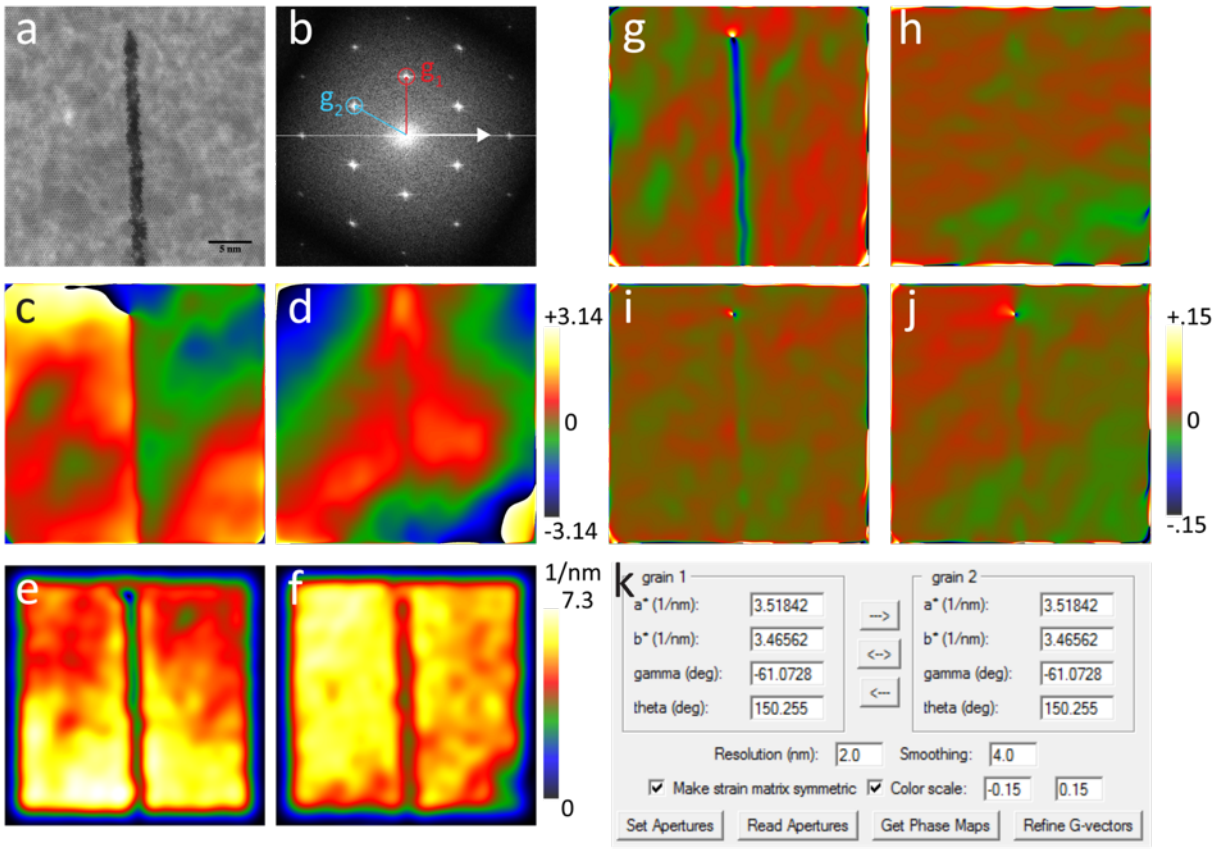

Figure C.1: Geometric phase analysis (GPA). (a) ADF-STEM showing the 1-D MoS_2 channel embedded within WSe_2. (b) The Fourier transform of a with apertures indicated by red and blue circles. (c, d) The geometric phase images calculated from g_1 and g_2 in (b). (e, f) The scale of the reciprocal lattice vectors g_1 and g_2 respectively. (g-j) The strain maps: ε_{xx}, ε_{yy}, ε_{xy}, and rotation respectively. (k) The screen capture of the control panel in the GPA plugin.

reciprocal lattice vectors g_1 and g_2, as shown in Fig. C.1 b in red and blue circles on the power spectrum. The size of the masks is smaller than the Brillouin zone. The resolution and smoothing setup in Fig. C.1 k define the size and smoothing of the masks, which help to reduce noise and smooth the resulting images.

3. Calculate the phase image: We convolved each region around reciprocal vector g_1 and g_2 with the masks. Afterwards, we performed an inversed

Fourier transform to create a complex image that the phase image was calculated from.

$$P_g(\mathbf{r}) = \arg[H'_g(\mathbf{r})] - 2\pi\mathbf{g}\cdot\mathbf{r} \tag{C.1}$$

where $H'_g(\mathbf{r})$ is complex image from the inversed Fourier transform, and $\mathbf{g}$ is the reciprocal lattice vector where the mask was placed. The phase images corresponding to reciprocal lattice vector g_1 and g_2 were plotted in Fig. C.1 c and d after a renormalization between $\pm\pi$.

4. Determine the displacement field: In the presence of a displacement field $\mathbf{u}$, the maximum of the fringes $\mathbf{r}$ is displaced by $\mathbf{u}$, and becomes $\mathbf{r} - \mathbf{u}$. In this case, we can write the intensity of Bragg filtered images that were produced by the Gaussian mask at $\mathbf{g}$:

$$\mathbf{u}(\mathbf{r}) = -\frac{1}{2\pi}[P_{g_1}(\mathbf{r})a_1 + P_{g2}(\mathbf{r})a_2] \tag{C.2}$$

where a_1 and a_2 are the inverse of g_1 and g_2.

5. Determine the strain and rotation fields: The local distortion of the lattice can be calculated from the gradient of the displacement field and defined as a 2 by 2 matrix:

$$e = \begin{bmatrix} e_{xx} & e_{xy} \\ e_{yx} & e_{yy} \end{bmatrix} = \begin{bmatrix} \frac{\partial u_x}{\partial x} & \frac{\partial u_x}{\partial y} \\ \frac{\partial u_y}{\partial x} & \frac{\partial u_y}{\partial y} \end{bmatrix} \tag{C.3}$$

The strain is given by the symmetric term $\varepsilon = \frac{1}{2}[e + e^T]$ and the rigid rotation is described by the anti-symmetric term $\omega = \frac{1}{2}[e - e^T]$. In this paper, the uniaxial strain can be calculated using $\varepsilon_{xx} = e_{xx}$, and $\varepsilon_{yy} = e_{yy}$, as shown in Fig. C.1 g and h respectively. The shear strain field map is shown in Fig. C.1 i calculated using $\varepsilon_{xy} = (e_{xy} + e_{yx})/2$. The rotation map displayed in Fig. C.1 j is calculated by $\varepsilon_{rot} = (e_{xy} - e_{yx})/2$.

In Fig. C.1 k, we cropped the GPA plugin control panel (downloaded from *https://www.physics.hu-berlin.de/en/sem/software/software_frwrtools*). In this software, 'a*' displays the length of reciprocal lattice vector g_1 in 1/nm unit and 'b*' shows that of g_2. The local $|g_1|$ and $|g_2|$ were mapped in Fig. C.1 e and f. Gamma represents the angle between g_1 and g_2 in degrees, while theta displays the angle between g_2 and the horizontal axis (white arrow in Fig. C.1 b). The resolution setup defines the size of the Gaussian masks and the smoothing defines the mask edge smoothing. The 'refined G-vectors' button calculate the **g** vectors in the reference lattice region we selected, thus refine the center of the masks. Here in this work we select the flat WSe_2 region as the reference lattice.

APPENDIX D

STRAIN MAPS USING EMPAD

D.1 CoM measurements

The CoM is calculated from the diffraction pattern, $I(\vec{p})$, using the following equation:

$$\langle \vec{p} \rangle = \int \vec{p} I(\vec{p}) d\vec{p} \tag{D.1}$$

where $\vec{p}$ is the momentum in the diffraction space.

Fig. D.1 shows the definition of our masks (green circles) that were applied to the diffraction disks and the center disk when we calculated their CoMs. The green dots label the calculated CoMs of all disks. Fig. D.1 c shows that the diffraction disk span across ~6 pixels in diameter. The mask with a diameter of 12 pixels is aligned to the disk with 1/3-pixel resolution by eye. We attempted aligning the mask as well as possible and, in fact, we achieved that the center of the mask is close to the measured CoM in Fig. D.1 d. In addition, measuring the centers for the EMPAD 4-D data, generally a few gigabytes in size, requires a fast-computational algorithm. The CoM calculation is an $O(n)$ algorithm, where n can usually be only tens of pixels for each diffraction disk. As a conclusion, CoM is a high-efficiency approach for measuring centers for the EMPAD 4-D datasets.

CoM has the advantage of speed and simplicity compared to more elaborate curve fitting procedures. The CoM provides sufficiently accurate centers of diffraction patterns of 2-D materials mainly because of the following two reasons: 1) the rod-like nature of diffraction patterns of 2-D materials and 2) the

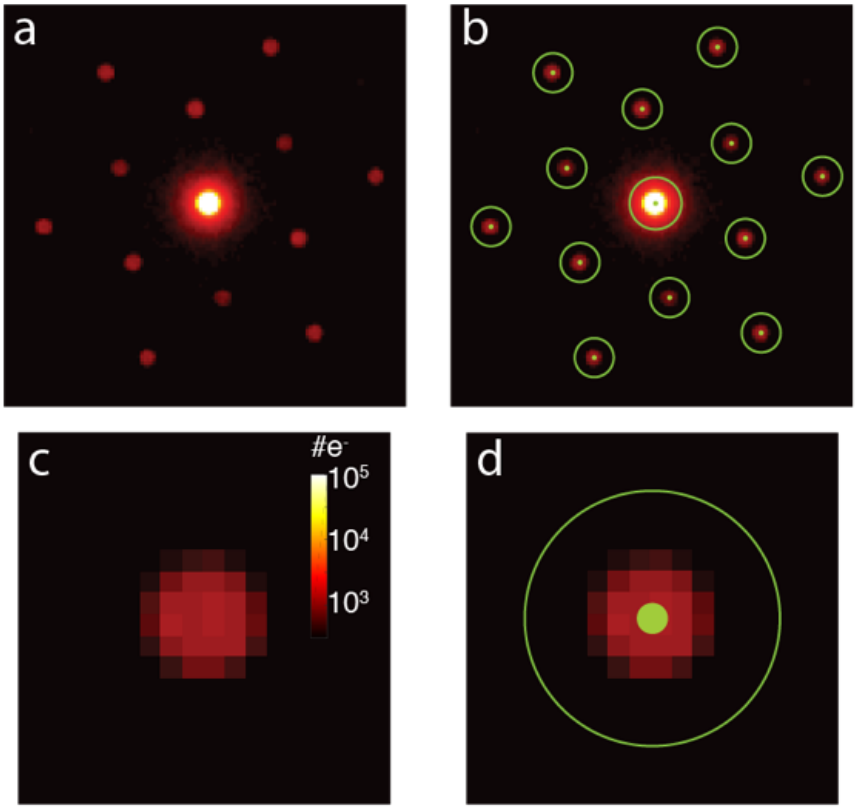

Figure D.1: CoM measurements. (a) A diffraction pattern of WS_2 on a 5 nm SiN_x window taken by EMPAD. (b) The diffraction pattern overlaid by the masks (green circles) and their CoMs (green dots). We manually placed the masks and aligned them to the diffraction spots by eye. (c,d) A magnified diffraction disk (c) and its overlay with the mask and the CoM (d).

high dynamic range of our EMPAD, which counts all transmitted electrons. The errors for CoM measurements come from the unavoidable Poisson noise from the detector.

Here, we discuss how Poisson noise affects the CoM. For each pixel in the EMPAD, the Poisson noise is proportional to the square root of the number of electrons hitting that pixel. By calculating the error propagation in Equ. D.1, we achieved that

$$\delta\text{CoM} = \sqrt{\frac{\langle p^2 \rangle}{I}} \tag{D.2}$$

where δCoM is the absolute error of CoM and I is the beam current. This result shows that reducing beam current will increase the error caused by Poisson noise, indicating that high beam current is preferred. However, there is a trade-off between high beam current for more accurate CoM and low beam current to avoid electron beam damage in 2-D materials. Experimentally, we were working with a beam current of 10 pA, and used a binning factor of 4 in real space, resulting a total of 2×10^6 electrons per frame and $\sim 10^4$ electrons in a second-order diffraction disk.

$\langle p^2 \rangle$ is the second moment which will be defined in Equ. D.10. The second moment is a measure of the beam broadness and has a unit of length square in the diffraction space. As a result, Equ. D.2 implies a linear growth of the error corresponding to the disk diameter. Fig. D.2 a shows the diffraction disks with different diameters, which can be measured in the unit of pixels of the detector. We simulated δCoM for different disk diameters by averaging the errors from 1,000 diffraction patterns with Poisson noise (Fig. D.2 b). The results indicate the absolute error (δCoM) is proportional to the disk diameter for a given dose.

There are two ways to reduce the disk diameters: decreasing the camera length (equivalent to building less pixels in the detector) or spread out the beam on the sample to focus the diffraction patterns in momentum space. We will discuss these two cases separately in the following sections.

D.1.1 Changing the camera length

The parameter determines the angular resolution is the percentage error, σ, which is the ratio between the absolute error (δCoM) and the k vector length:

$$\sigma = \delta CoM/k \tag{D.3}$$

We note that k, as well as the disk diameter, changes correspondingly as we change the pixel size in the detector (or change the camera length to magnify or demagnify the diffraction patterns), as shown in Fig. D.2 c. In addition, since k is proportional to the disk diameter, here, we ignored a constant scaling prefactor, assumed k equals to the disk diameter, and plotted the percentage errors in Fig. D.2 d. The percentage errors are close to a constant with small increment at the smaller disk diameters, especially for the low-dose case. For example, if each diffraction disk only contains 10 electrons (blue curve in Fig. D.2 d), we would choose 10-15 pixels for a disk diameter for reasonable angular resolution. For doses larger than 1,000 electrons per disk, where we worked at, the optimized disk diameters will be any one larger than 5 pixels. Above that, the errors stay constant, indicating that we do not benefit from designing more pixels in the detector or magnifying the diffraction patterns.

D.1.2 Changing the convergence angle

For diffraction disks at a fixed camera length and pixel size (k is fixed), the disk diameter is proportional to the convergence angle θ. Thus, the percentage error becomes:

$$\sigma \propto \frac{\theta}{\sqrt{I}} \tag{D.4}$$

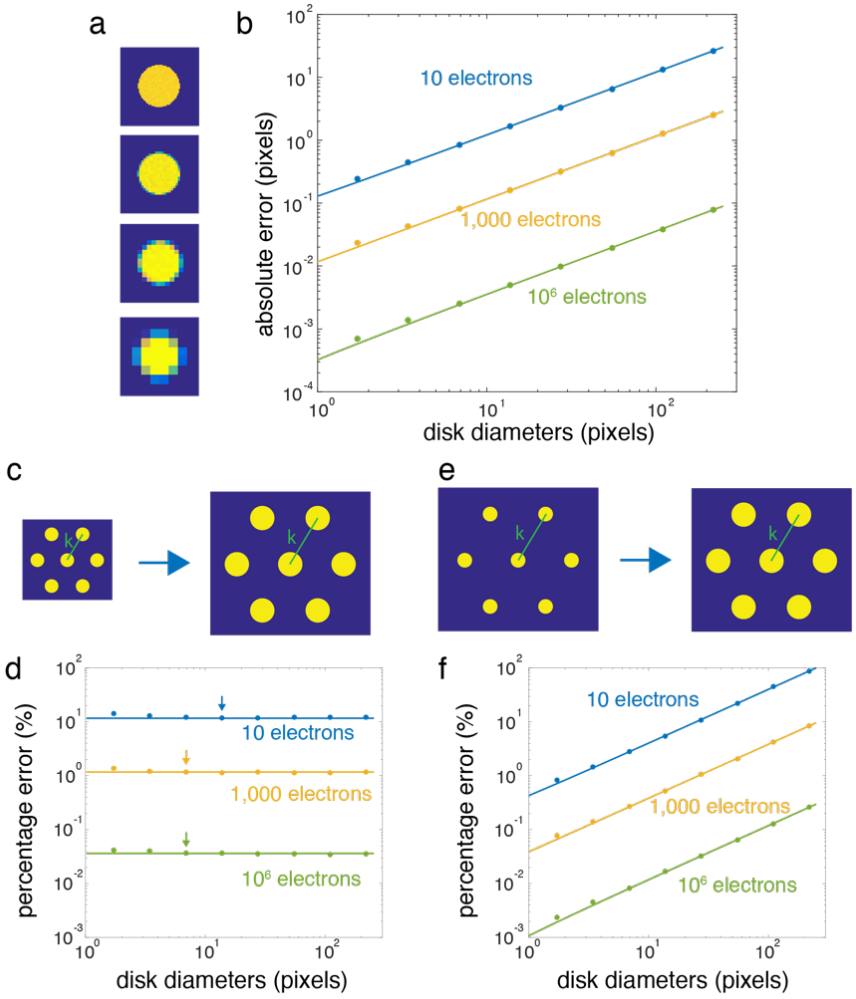

Figure D.2: Accuracy of CoM measurements. (a) Simulated diffraction patterns of different diameters (in pixels) with Poisson noise. (b) Absolute errors of CoM (δCoM) proportional to the disk diameters. (c) Schematics of diffraction patterns when we increase the number of pixels in the detector (or magnify the diffraction patterns by changing the camera length). (d) Percentage error plot (δCoM/k) under the situation described in (c), with arrows indicating the lower bounds of the optimized disk diameters. (We used k = disk diameter.) (e) Schematics of diffraction patterns when we change the convergence angle. (f) Percentage error plot (δ CoM/k) for cases in (e), showing that reducing the convergence angle will reduce the error and improve the angular resolution dramatically. (We used k = 30 pixels.)

Smaller convergence angles lead to less percentage errors (as shown in Fig. D.2 e and f). This means more parallel beam is preferred. The lower bound is a 2×2-pixel-sized diffraction disk, which is similar to a DPC detector.

However, in STEM mode, the spatial resolution is determined by the spot size. For a diffraction-limited probe, there is a trade-off between the spatial resolution and the angular resolution in k space. Reducing the convergence angle (improving the angular resolution) will decrease the spot size:

$$d_0 = 1.22\frac{\lambda}{\theta} \tag{D.5}$$

where d_0 is the spot size and λ is the wavelength of the electrons. Combining Equ. D.4 and D.5 gives the relationship:

$$\theta \propto \frac{1}{d_0 \times \sqrt{I}} \tag{D.6}$$

where improving the spatial resolution (reducing d_0) will cause a reduction of the mapping precision for the same dose or it requires a square-dependence increment of the current to compensate.

D.2 Mapping lattice constants

To calculate the lattice constants from a single diffraction pattern, we averaged the distances between diffracting beams and the center beam, d_1 to d_6, as shown in Fig. D.3. The averaged lattice constant is:

$$a_{ave} = \frac{6a_0d_0}{\sum_{i=1}^{6} d_i} \tag{D.7}$$

where a_0 and d_0 are the calibrated ones from a referenced region. We used flat WS_2 as the reference.

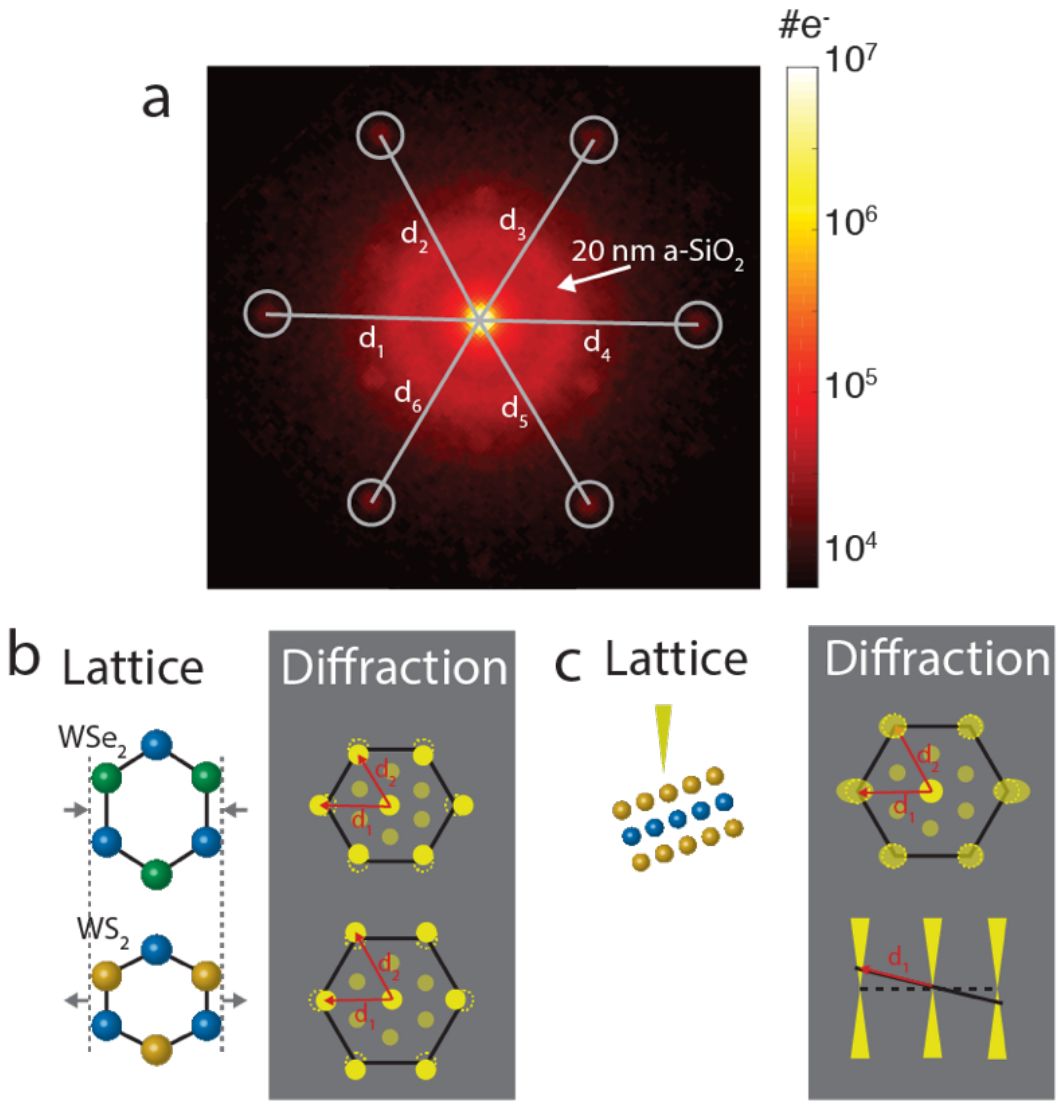

Figure D.3: Lattice constant map. (a) Diffraction pattern of WS_2-WSe_2 on 20 nm SiN_x windows. The gray circles are the masks we used to calculate the CoMs. The reciprocal lattice constants were measured, shown as d_1-d_6. (b) Schematic showing how strain affects the lattice constant measurements. (c) Schematic showing how small tilt affects the lattice constant measurements. The small strain and tilt are higher order effect for lattice constant calculation.

In STEM, EMPAD acquires diffraction patterns at each scan position with 1.86 ms/frame (1 ms exposure time and 0.86 ms readout time) so a 4-D data (x and y in real space and k_x and k_y in momentum space) at 256×256 scan points can be reached in about two minutes. Using the 4-D dataset, we can map the lattice constant throughout the entire sample.

Although there are strain and tilt at some regions in the sample, due to the averaging of the six spots in different directions, the strain and tilt effects are negligible. Fig. D.3 b and c show the schematics of how strain and tilt affect the diffraction pattern. The calculation below describes that the strain and tilt are higher order effects in the lattice constant calculation:

$$a'_{ave} \cong \frac{3a_0d_0}{d_1(1+\varepsilon') + 2d_2\left(1 - \frac{\sqrt{3}}{2}\nu\varepsilon'\right)} \tag{D.8}$$

where ν is the Poissons ratio (0.25 for WS_2) and ε' is a small uniaxial strain. (we used compressive strain here.)

$$a''_{ave} \cong \frac{3a_0d_0}{d_1(1+\frac{\theta^2}{2}) + 2d_2\left(1 + \frac{\theta^2}{8}\right)} \tag{D.9}$$

where θ is the small tilt angle.

D.3 Mapping strain

To map the strain from the 4-D dataset, we calculated the diffraction vectors $g_i (i = 1, 2)$ (i.e. the reciprocal lattice vectors) as shown in Fig. D.4 a. The reference diffraction vectors g_i^{ref} were set by averaging 200 scan positions (or pixels) in real space where half of them are on WS_2 and the other half are on the

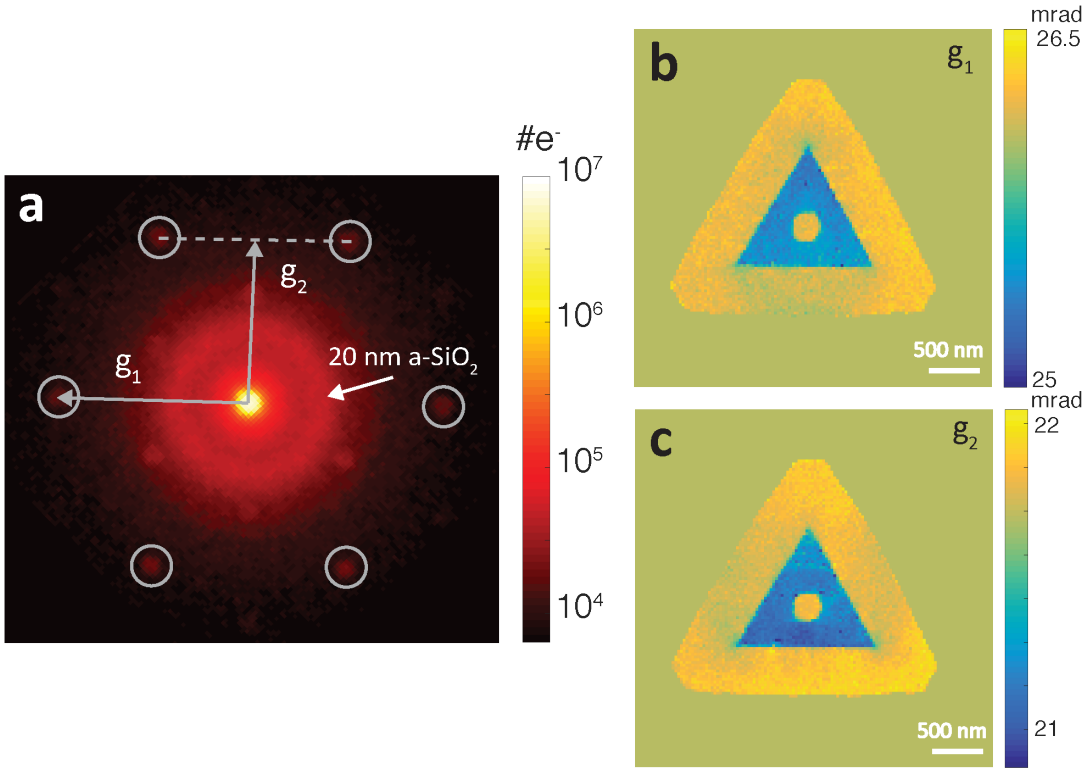

Figure D.4: Maps of diffraction vectors. (a) A single diffraction pattern of WSe_2 taken by EMPAD with second order diffraction spots highlighted by the masks. For each spot, we calculated the CoM and achieve the diffraction vectors as labeled by g_1 and g_2. (b,c) $|g_1|$ and $|g_2|$ maps over the entire triangle.

WSe_2. The choice of these g_i^{ref} is for mapping convenience. Afterwards, we derived the transformation matrix T using $g_i = Tg_i^{ref}$. T can be polar-decomposed into a rotation matrix R and a strain matrix U, from which the uniaxial strain $\varepsilon_{xx} = 1 - U_{11}$ and $\varepsilon_{yy} = 1 - U_{22}$, shear strain $\varepsilon_{xy} = U_{12}$, and rotation $\varepsilon_{rot} = asin(R_{12})$ can be calculated.

D.4 Mapping ripples

Second moments are the variance, which describes the broadness of the diffraction spots. For the x-component of momentum transfer, we have:

$$\langle p_x^2 \rangle = \int p_x^2 I(\vec{p}) d\vec{p} \tag{D.10}$$

We computed the second moments using the same masks we used for CoM calculation. From the calculated second moments for all diffraction spots, the broadness of each diffraction spot is

$$A(\text{or } B, C) = \sqrt{\langle p_x^2 \rangle + \langle p_y^2 \rangle} \tag{D.11}$$

where the A, B, and C are the corresponding second moments of the diffraction spots in Fig. 3.4 a. To plot rotational ripple maps, we defined the complex ripple measure:

$$R = A + Be^{i2\pi/3} + ce^{i4\pi/3} \tag{D.12}$$

The phase of R represents the direction (or orientation) of the ripple line, while the amplitude shows the tilt angle of the ripples.

To quantify the tilt angle, we can plot the projection of R along the tilt direction

$$\text{Re}\,[R] = A - 0.5B - 0.5C \tag{D.13}$$

whose intensity is proportional to the tilt angle.

BIBLIOGRAPHY

[1] Gordon E. Moore. Cramming more components onto integrated circuits. *Electronics*, 38(8):114–117, 1965.

[2] Robert Chau, Brian Doyle, Suman Datta, Jack Kavalieros, and Kevin Zhang. Integrated nanoelectronics for the future. *Nature materials*, 6(11):810, 2007.

[3] David K Ferry. Nanowires in nanoelectronics. *Science*, 319(5863):579–580, 2008.

[4] Thomas N Theis and Paul M Solomon. Its time to reinvent the transistor! *Science*, 327(5973):1600–1601, 2010.

[5] Aaron D Franklin. Nanomaterials in transistors: From high-performance to thin-film applications. *Science*, 349(6249):aab2750, 2015.

[6] Kostya S Novoselov, Andre K Geim, SVb Morozov, Da Jiang, MIc Katsnelson, IVa Grigorieva, SVb Dubonos, Firsov, and AA. Two-dimensional gas of massless dirac fermions in graphene. *Nature*, 438(7065):197, 2005.

[7] Kostya S Novoselov, Andre K Geim, Sergei V Morozov, D Jiang, Y_ Zhang, Sergey V Dubonos, Irina V Grigorieva, and Alexandr A Firsov. Electric field effect in atomically thin carbon films. *Science*, 306(5696):666–669, 2004.

[8] Yuanbo Zhang, Yan-Wen Tan, Horst L Stormer, and Philip Kim. Experimental observation of the quantum hall effect and berry's phase in graphene. *Nature*, 438(7065):201, 2005.

[9] Andre K Geim and Konstantin S Novoselov. The rise of graphene. *Nature materials*, 6(3):183, 2007.

[10] H Fernandezmoran. Single-crystals of graphite and of mica as specimen supports for electron microscopy. *Journal of Applied Physics*, 31(10):1840, 1960.

[11] BV Johansen. Bright field electron microscopy of biological specimensiv. ultrasonic exfoliated graphite as low-noisesupport films. *Micron*, 6(3-4):165–173, 1975.

[12] Sumio Iijima. Thin graphite supporting films for high resolution work. In *34th Ann. Proc. EMSA*, page 568, 1976.

[13] Kin Fai Mak, Changgu Lee, James Hone, Jie Shan, and Tony F Heinz. Atomically thin mos 2: a new direct-gap semiconductor. *Physical review letters*, 105(13):136805, 2010.

[14] Branimir Radisavljevic, Aleksandra Radenovic, Jacopo Brivio, i V Giacometti, and A Kis. Single-layer mos 2 transistors. *Nature nanotechnology*, 6(3):147, 2011.

[15] Kin Fai Mak, Kathryn L McGill, Jiwoong Park, and Paul L McEuen. The valley hall effect in mos2 transistors. *Science*, 344(6191):1489–1492, 2014.

[16] Sujay B Desai, Surabhi R Madhvapathy, Angada B Sachid, Juan Pablo Llinas, Qingxiao Wang, Geun Ho Ahn, Gregory Pitner, Moon J Kim, Jeffrey Bokor, Chenming Hu, et al. Mos2 transistors with 1-nanometer gate lengths. *Science*, 354(6308):99–102, 2016.

[17] Yuan Cao, Valla Fatemi, Shiang Fang, Kenji Watanabe, Takashi Taniguchi, Efthimios Kaxiras, and Pablo Jarillo-Herrero. Unconventional superconductivity in magic-angle graphene superlattices. *Nature*, 2018.

[18] Sukang Bae, Hyeongkeun Kim, Youngbin Lee, Xiangfan Xu, Jae-Sung Park, Yi Zheng, Jayakumar Balakrishnan, Tian Lei, Hye Ri Kim, Young Il Song, et al. Roll-to-roll production of 30-inch graphene films for transparent electrodes. *Nature nanotechnology*, 5(8):574, 2010.

[19] Yi-Hsien Lee, Xin-Quan Zhang, Wenjing Zhang, Mu-Tung Chang, Cheng-Te Lin, Kai-Di Chang, Ya-Chu Yu, Jacob Tse-Wei Wang, Chia-Seng Chang, Lain-Jong Li, et al. Synthesis of large-area mos2 atomic layers with chemical vapor deposition. *Advanced materials*, 24(17):2320–2325, 2012.

[20] Jae-Hyun Lee, Eun Kyung Lee, Won-Jae Joo, Yamujin Jang, Byung-Sung Kim, Jae Young Lim, Soon-Hyung Choi, Sung Joon Ahn, Joung Real Ahn, Min-Ho Park, et al. Wafer-scale growth of single-crystal monolayer graphene on reusable hydrogen-terminated germanium. *Science*, 344(6181):286–289, 2014.

[21] Xi Ling, Yi-Hsien Lee, Yuxuan Lin, Wenjing Fang, Lili Yu, Mildred S Dresselhaus, and Jing Kong. Role of the seeding promoter in mos2 growth by chemical vapor deposition. *Nano letters*, 14(2):464–472, 2014.

[22] Kibum Kang, Saien Xie, Lujie Huang, Yimo Han, Pinshane Y Huang, Kin Fai Mak, Cheol-Joo Kim, David Muller, and Jiwoong Park. High-mobility three-atom-thick semiconducting films with wafer-scale homogeneity. *Nature*, 520(7549):656, 2015.

[23] LD Landau. Zur theorie der phasenumwandlungen ii. *Phys. Z. Sowjetunion*, 11(545):26–35, 1937.

[24] Andre K Geim and Philip Kim. Carbon wonderland. *Scientific American*, 298(4):90–97, 2008.

[25] Jun Kang, Sefaattin Tongay, Jian Zhou, Jingbo Li, and Junqiao Wu. Band offsets and heterostructures of two-dimensional semiconductors. *Applied Physics Letters*, 102(1):012111, 2013.

[26] Pinshane Y Huang, Carlos S Ruiz-Vargas, Arend M van der Zande, William S Whitney, Mark P Levendorf, Joshua W Kevek, Shivank Garg, Jonathan S Alden, Caleb J Hustedt, Ye Zhu, et al. Grains and grain boundaries in single-layer graphene atomic patchwork quilts. *Nature*, 469(7330):389, 2011.

[27] Adam W Tsen, Lola Brown, Mark P Levendorf, Fereshte Ghahari, Pinshane Y Huang, Robin W Havener, Carlos S Ruiz-Vargas, David A Muller, Philip Kim, and Jiwoong Park. Tailoring electrical transport across grain boundaries in polycrystalline graphene. *Science*, 336(6085):1143–1146, 2012.

[28] Arend M Van Der Zande, Pinshane Y Huang, Daniel A Chenet, Timothy C Berkelbach, YuMeng You, Gwan-Hyoung Lee, Tony F Heinz, David R Reichman, David A Muller, and James C Hone. Grains and grain boundaries in highly crystalline monolayer molybdenum disulphide. *Nature materials*, 12(6):554, 2013.

[29] Xiaolong Zou, Yuanyue Liu, and Boris I Yakobson. Predicting dislocations and grain boundaries in two-dimensional metal-disulfides from the first principles. *Nano letters*, 13(1):253–258, 2012.

[30] Wu Zhou, Xiaolong Zou, Sina Najmaei, Zheng Liu, Yumeng Shi, Jing Kong, Jun Lou, Pulickel M Ajayan, Boris I Yakobson, and Juan-Carlos Idrobo. Intrinsic structural defects in monolayer molybdenum disulfide. *Nano letters*, 13(6):2615–2622, 2013.

[31] Amin Azizi, Xiaolong Zou, Peter Ercius, Zhuhua Zhang, Ana Laura Elías, Néstor Perea-López, Greg Stone, Mauricio Terrones, Boris I Yakobson, and

Nasim Alem. Dislocation motion and grain boundary migration in two-dimensional tungsten disulphide. *Nature communications*, 5:4867, 2014.

[32] Yung-Chang Lin, Torbjörn Björkman, Hannu-Pekka Komsa, Po-Yuan Teng, Chao-Hui Yeh, Fei-Sheng Huang, Kuan-Hung Lin, Joanna Jadczak, Ying-Sheng Huang, Po-Wen Chiu, et al. Three-fold rotational defects in two-dimensional transition metal dichalcogenides. *Nature communications*, 6:6736, 2015.

[33] Jinhua Hong, Chuanhong Jin, Jun Yuan, and Ze Zhang. Atomic defects in two-dimensional materials: From single-atom spectroscopy to functionalities in opto-/electronics, nanomagnetism, and catalysis. *Advanced Materials*, 2017.

[34] Derek Hull and David J Bacon. *Introduction to dislocations*, volume 37. Elsevier, 2011.

[35] Chul-Ho Lee, Gwan-Hyoung Lee, Arend M Van Der Zande, Wenchao Chen, Yilei Li, Minyong Han, Xu Cui, Ghidewon Arefe, Colin Nuckolls, Tony F Heinz, et al. Atomically thin p–n junctions with van der waals heterointerfaces. *Nature nanotechnology*, 9(9):676, 2014.

[36] Yongji Gong, Junhao Lin, Xingli Wang, Gang Shi, Sidong Lei, Zhong Lin, Xiaolong Zou, Gonglan Ye, Robert Vajtai, Boris I Yakobson, et al. Vertical and in-plane heterostructures from ws 2/mos 2 monolayers. *Nature materials*, 13(12):1135, 2014.

[37] Xidong Duan, Chen Wang, Jonathan C Shaw, Rui Cheng, Yu Chen, Honglai Li, Xueping Wu, Ying Tang, Qinling Zhang, Anlian Pan, et al. Lateral epitaxial growth of two-dimensional layered semiconductor heterojunctions. *Nature nanotechnology*, 9(12):1024, 2014.

[38] Chunming Huang, Sanfeng Wu, Ana M Sanchez, Jonathan JP Peters, Richard Beanland, Jason S Ross, Pasqual Rivera, Wang Yao, David H Cobden, and Xiaodong Xu. Lateral heterojunctions within monolayer mose 2–wse 2 semiconductors. *Nature materials*, 13(12):1096, 2014.

[39] Ming-Yang Li, Yumeng Shi, Chia-Chin Cheng, Li-Syuan Lu, Yung-Chang Lin, Hao-Lin Tang, Meng-Lin Tsai, Chih-Wei Chu, Kung-Hwa Wei, Jr-Hau He, et al. Epitaxial growth of a monolayer wse2-mos2 lateral pn junction with an atomically sharp interface. *Science*, 349(6247):524–528, 2015.

[40] Yongji Gong, Sidong Lei, Gonglan Ye, Bo Li, Yongmin He, Kunttal Keyshar, Xiang Zhang, Qizhong Wang, Jun Lou, Zheng Liu, et al. Two-step growth of two-dimensional wse2/mose2 heterostructures. *Nano letters*, 15(9):6135–6141, 2015.

[41] Xi Ling, Yuxuan Lin, Qiong Ma, Ziqiang Wang, Yi Song, Lili Yu, Shengxi Huang, Wenjing Fang, Xu Zhang, Allen L Hsu, et al. Parallel stitching of 2d materials. *Advanced Materials*, 28(12):2322–2329, 2016.

[42] Mervin Zhao, Yu Ye, Yimo Han, Yang Xia, Hanyu Zhu, Siqi Wang, Yuan Wang, David A Muller, and Xiang Zhang. Large-scale chemical assembly of atomically thin transistors and circuits. *Nature nanotechnology*, 11(11):954, 2016.

[43] Marcos HD Guimaraes, Hui Gao, Yimo Han, Kibum Kang, Saien Xie, Cheol-Joo Kim, David A Muller, Daniel C Ralph, and Jiwoong Park. Atomically thin ohmic edge contacts between two-dimensional materials. *ACS nano*, 10(6):6392–6399, 2016.

[44] Mark P Levendorf, Cheol-Joo Kim, Lola Brown, Pinshane Y Huang, Robin W Havener, David A Muller, and Jiwoong Park. Graphene and boron nitride lateral heterostructures for atomically thin circuitry. *Nature*, 488(7413):627, 2012.

[45] Lei Liu, Jewook Park, David A Siegel, Kevin F McCarty, Kendal W Clark, Wan Deng, Leonardo Basile, Juan Carlos Idrobo, An-Ping Li, and Gong Gu. Heteroepitaxial growth of two-dimensional hexagonal boron nitride templated by graphene edges. *Science*, 343(6167):163–167, 2014.

[46] Lingxiu Chen, Li He, Hui Shan Wang, Haomin Wang, Shujie Tang, Chunxiao Cong, Hong Xie, Lei Li, Hui Xia, Tianxin Li, et al. Oriented graphene nanoribbons embedded in hexagonal boron nitride trenches. *Nature communications*, 8:14703, 2017.

[47] Zhengwei Zhang, Peng Chen, Xidong Duan, Ketao Zang, Jun Luo, and Xiangfeng Duan. Robust epitaxial growth of two-dimensional heterostructures, multiheterostructures, and superlattices. *Science*, 357(6353):788–792, 2017.

[48] Yimo Han, Ming-Yang Li, Gang-Seob Jung, Mark A Marsalis, Zhao Qin, Markus J Buehler, Lain-Jong Li, and David A Muller. Sub-nanometre channels embedded in two-dimensional materials. *Nature materials*, 17(2):129, 2018.

[49] Saien Xie, Lijie Tu, Yimo Han, Lujie Huang, Kibum Kang, Ka Un Lao, Preeti Poddar, Chibeom Park, David A Muller, Robert A DiStasio, et al. Coherent, atomically thin transition-metal dichalcogenide superlattices with engineered strain. *Science*, 359(6380):1131–1136, 2018.

[50] Yimo Han, Kayla Nguyen, Michael Cao, Paul Cueva, Saien Xie, Mark W Tate, Prafull Purohit, Sol M Gruner, Jiwoong Park, and David A Muller. Strain mapping of two-dimensional heterostructures with sub-picometer precision. *arXiv preprint arXiv:1801.08053*, 2018.

[51] Andre K Geim and Irina V Grigorieva. Van der waals heterostructures. *Nature*, 499(7459):419, 2013.

[52] E Fred Schubert. Light-emitting diodes. *Light-Emitting Diodes-2nd Edition, by E. Fred Schubert, pp. 432. Cambridge University Press, June 2006. ISBN-10: 0521865387. ISBN-13: 9780521865388. LCCN: TK7871. 89. L53. S47 2006*, page 432, 2006.

[53] Manfred Von Ardenne. Das elektronen-rastermikroskop. *Zeitschrift für Physik*, 109(9-10):553–572, 1938.

[54] AV Crewe, J Wall, and LM Welter. A high-resolution scanning transmission electron microscope. *Journal of Applied Physics*, 39(13):5861–5868, 1968.

[55] Robert J Keyse. *Introduction to scanning transmission electron microscopy*. BIOS Scientific Publishers in association with the Royal Microscopical Society, 1998.

[56] Max Knoll and Ernst Ruska. Das elektronenmikroskop. *Zeitschrift für Physik*, 78(5-6):318–339, 1932.

[57] M Weyland and DA Muller. Tuning the convergence angle for optimum stem performance. *FEI Nanosolutions*, 1:24–35, 2005.

[58] OL Krivanek, N Dellby, and AR Lupini. Towards sub- electron beams. *Ultramicroscopy*, 78(1-4):1–11, 1999.

[59] OL Krivanek, GJ Corbin, N Dellby, BF Elston, RJ Keyse, MF Murfitt, CS Own, ZS Szilagyi, and JW Woodruff. An electron microscope for the aberration-corrected era. *Ultramicroscopy*, 108(3):179–195, 2008.

[60] Earl J Kirkland. On the optimum probe in aberration corrected adf-stem. *Ultramicroscopy*, 111(11):1523–1530, 2011.

[61] M Haider, S Uhlemann, and J Zach. Upper limits for the residual aberrations of a high-resolution aberration-corrected stem. *Ultramicroscopy*, 81(3-4):163–175, 2000.

[62] Heiko Müller, Stephan Uhlemann, Peter Hartel, and Maximilian Haider. Advancing the hexapole c s-corrector for the scanning transmission electron microscope. *Microscopy and Microanalysis*, 12(6):442–455, 2006.

[63] Ondrej L Krivanek, Niklas Dellby, Matthew F Murfitt, Matthew F Chisholm, Timothy J Pennycook, Kazutomo Suenaga, and Valeria Nicolosi. Gentle stem: Adf imaging and eels at low primary energies. *Ultramicroscopy*, 110(8):935–945, 2010.

[64] Kibum Kang, Kan-Heng Lee, Yimo Han, Hui Gao, Saien Xie, David A Muller, and Jiwoong Park. Layer-by-layer assembly of two-dimensional materials into wafer-scale heterostructures. *Nature*, 550(7675):229, 2017.

[65] Ang-Yu Lu, Hanyu Zhu, Jun Xiao, Chih-Piao Chuu, Yimo Han, Ming-Hui Chiu, Chia-Chin Cheng, Chih-Wen Yang, Kung-Hwa Wei, Yiming Yang, et al. Janus monolayers of transition metal dichalcogenides. *Nature nanotechnology*, 12(8):744, 2017.

[66] Yutsung Tsai, Zhaodong Chu, Yimo Han, Chih-Piao Chuu, Di Wu, Alex Johnson, Fei Cheng, Mei-Yin Chou, David A Muller, Xiaoqin Li, et al. Tailoring semiconductor lateral multijunctions for giant photoconductivity enhancement. *Advanced Materials*, 29(41), 2017.

[67] Ondrej L Krivanek, Matthew F Chisholm, Valeria Nicolosi, Timothy J Pennycook, George J Corbin, Niklas Dellby, Matthew F Murfitt, Christopher S Own, Zoltan S Szilagyi, Mark P Oxley, et al. Atom-by-atom structural and chemical analysis by annular dark-field electron microscopy. *Nature*, 464(7288):571, 2010.

[68] David A Muller, Kayla X Nguyen, Mark W Tate, Prafull Purohit, Celesta Chang, Michael Cao, and Sol M Gruner. An electron microscope pixel array detector as a universal stem detector. *Microscopy and Microanalysis*, 22:478, 2016.

[69] Michael C Cao, Yimo Han, Zhen Chen, Yi Jiang, Kayla X Nguyen, Emrah

Turgut, Gregory D Fuchs, and David A Muller. Theory and practice of electron diffraction from single atoms and extended objects using an empad. *Microscopy*, 67(suppl_1):i150–i161, 2018.

[70] Eric GT Bosch, Ivan Lazic, and Sorin Lazar. Integrated differential phase contrast (idpc) stem: A new atomic resolution stem technique to image all elements across the periodic table. *Microscopy and Microanalysis*, 22:306, 2016.

[71] Yi Jiang, Zhen Chen, Yimo Han, Pratiti Deb, Hui Gao, Saien Xie, Prafull Purohit, Mark W Tate, Jiwoong Park, Sol M Gruner, et al. Deep sub-*a* ngstrom imaging of 2d materials with a high dynamic range detector. *arXiv preprint arXiv:1801.04630*, 2018.

[72] Kayla X Nguyen, Robert Hovden, Mark W Tate, Prafull Purohit, John Heron, Celesta Chang, Sol M Gruner, and David A Muller. Lorentz-stem imaging of fields and domains using a high-speed, high-dynamic range pixel array detector at atomic resolution. *Microscopy and Microanalysis*, 21:2309, 2015.

[73] Kayla X Nguyen, Prafull Purohit, Ajay Yadav, Mark W Tate, Celesta S Chang, Ramamoorthy Ramesh, Sol M Gruner, and David A Muller. Reconstruction of polarization vortices by diffraction mapping of ferroelectric pbtio3/srtio3 superlattice using a high dynamic range pixelated detector. *Microscopy and Microanalysis*, 22:472, 2016.

[74] Rui Cheng, Dehui Li, Hailong Zhou, Chen Wang, Anxiang Yin, Shan Jiang, Yuan Liu, Yu Chen, Yu Huang, and Xiangfeng Duan. Electroluminescence and photocurrent generation from atomically sharp wse2/mos2 heterojunction p–n diodes. *Nano letters*, 14(10):5590–5597, 2014.

[75] Tania Roy, Mahmut Tosun, Xi Cao, Hui Fang, Der-Hsien Lien, Peida Zhao, Yu-Ze Chen, Yu-Lun Chueh, Jing Guo, and Ali Javey. Dual-gated mos2/wse2 van der waals tunnel diodes and transistors. *Acs Nano*, 9(2):2071–2079, 2015.

[76] Chendong Zhang, Ming-Yang Li, Jerry Tersoff, Yimo Han, Yushan Su, Lain-Jong Li, David A Muller, and Chih-Kang Shih. Strain distributions and their influence on electronic structures of wse 2–mos 2 laterally strained heterojunctions. *Nature nanotechnology*, page 1, 2018.

[77] MJ Hÿtch, E Snoeck, and R Kilaas. Quantitative measurement of displace-

ment and strain fields from hrem micrographs. *Ultramicroscopy*, 74(3):131–146, 1998.

[78] Yu Li Huang, Yifeng Chen, Wenjing Zhang, Su Ying Quek, Chang-Hsiao Chen, Lain-Jong Li, Wei-Ting Hsu, Wen-Hao Chang, Yu Jie Zheng, Wei Chen, et al. Bandgap tunability at single-layer molybdenum disulphide grain boundaries. *Nature communications*, 6:6298, 2015.

[79] Fumihiko Uesugi, Akira Hokazono, and Shiro Takeno. Evaluation of two-dimensional strain distribution by stem/nbd. *Ultramicroscopy*, 111(8):995–998, 2011.

[80] Knut Müller, Andreas Rosenauer, Marco Schowalter, Josef Zweck, Rafael Fritz, and Kerstin Volz. Strain measurement in semiconductor heterostructures by scanning transmission electron microscopy. *Microscopy and Microanalysis*, 18(5):995–1009, 2012.

[81] Jian Min Zuo and John CH Spence. Strain measurements and mapping. In *Advanced Transmission Electron Microscopy*, pages 553–580. Springer, 2017.

[82] VB Ozdol, C Gammer, XG Jin, P Ercius, C Ophus, J Ciston, and AM Minor. Strain mapping at nanometer resolution using advanced nano-beam electron diffraction. *Applied Physics Letters*, 106(25):253107, 2015.

[83] Thomas C Pekin, Christoph Gammer, Jim Ciston, Andrew M Minor, and Colin Ophus. Optimizing disk registration algorithms for nanobeam electron diffraction strain mapping. *Ultramicroscopy*, 176:170–176, 2017.

[84] AG Cullis, DJ Robbins, SJ Barnett, and AJ Pidduck. Growth ripples upon strained sige epitaxial layers on si and misfit dislocation interactions. *Journal of Vacuum Science & Technology A: Vacuum, Surfaces, and Films*, 12(4):1924–1931, 1994.

[85] Jannik C Meyer, Andre K Geim, Mikhail I Katsnelson, Konstantin S Novoselov, Tim J Booth, and Siegmar Roth. The structure of suspended graphene sheets. *Nature*, 446(7131):60, 2007.

[86] Yumeng Shi, Wu Zhou, Ang-Yu Lu, Wenjing Fang, Yi-Hsien Lee, Allen Long Hsu, Soo Min Kim, Ki Kang Kim, Hui Ying Yang, Lain-Jong Li, et al. van der waals epitaxy of mos2 layers using graphene as growth templates. *Nano letters*, 12(6):2784–2791, 2012.

[87] Melina K Blees, Arthur W Barnard, Peter A Rose, Samantha P Roberts, Kathryn L McGill, Pinshane Y Huang, Alexander R Ruyack, Joshua W Kevek, Bryce Kobrin, David A Muller, et al. Graphene kirigami. *Nature*, 524(7564):204, 2015.

[88] Marc Z Miskin, Kyle J Dorsey, Baris Bircan, Yimo Han, David A Muller, Paul L McEuen, and Itai Cohen. Graphene-based bimorphs for micron-sized, autonomous origami machines. *Proceedings of the National Academy of Sciences*, 115(3):466–470, 2018.

[89] Lucille A Giannuzzi et al. *Introduction to focused ion beams: instrumentation, theory, techniques and practice*. Springer Science & Business Media, 2004.

[90] Cory R Dean, Andrea F Young, Inanc Meric, Chris Lee, Lei Wang, Sebastian Sorgenfrei, Kenji Watanabe, Takashi Taniguchi, Phillip Kim, Kenneth L Shepard, et al. Boron nitride substrates for high-quality graphene electronics. *Nature nanotechnology*, 5(10):722, 2010.

[91] L Wang, I Meric, PY Huang, Q Gao, Y Gao, H Tran, T Taniguchi, K Watanabe, LM Campos, DA Muller, et al. One-dimensional electrical contact to a two-dimensional material. *Science*, 342(6158):614–617, 2013.